

1 **Satellite observations of cirrus clouds in the northern**
2 **hemisphere lowermost stratosphere**

3

4 **R. Spang¹, G. Günther¹, M. Riese¹, L. Hoffmann², R. Müller¹, and S. Griessbach²**

5

6 [1]{Forschungszentrum Jülich, Institut für Energie and Klimaforschung, IEK-7, Jülich,
7 Germany}

8 [2]{Forschungszentrum Jülich, Jülich Supercomputing Centre, JSC, Jülich, Germany}

9

10

11 Correspondence to: R. Spang (r.spang@fz-juelich.de)

12

1 **Abstract**

2 Here we present observations of the Cryogenic Infrared Spectrometers and Telescopes for the
3 Atmosphere (CRISTA) of cirrus cloud and water vapour in August 1997 in the upper
4 troposphere and lower stratosphere (UTLS) region. The observations indicate a considerable
5 flux of moisture from the upper tropical troposphere into the extra-tropical lowermost
6 stratosphere (LMS), resulting in the occurrence of high altitude optically thin cirrus clouds in
7 the LMS.

8 The locations of the LMS cloud events observed by CRISTA are consistent with the
9 tropopause height determined from coinciding radiosonde data. For a hemispheric analysis in
10 tropopause relative coordinates an improved tropopause determination has been applied to the
11 ECMWF temperature profiles. We found that a significant fraction of the cloud occurrences
12 in the tropopause region are located in the LMS, even if a conservative overestimate of the
13 cloud top height (CTH) determination by CRISTA of 500 m is assumed. The results show
14 rather high occurrence frequencies (~5%) up to high northern latitudes (70°N) and altitudes
15 well above the tropopause (>500 m at ~350 K and above) in large areas at mid and high
16 latitudes.

17 Comparisons with model runs of the Chemical Lagrangian Model of the Stratosphere (CLaMS)
18 over the CRISTA period show a reasonable consistency for the retrieved cloud pattern. For
19 this purpose a limb ray tracing approach was applied through the 3D model fields to obtain
20 integrated measurement information through the atmosphere along the limb path of the
21 instrument. The simplified cirrus scheme implemented in CLaMS seems to cause a systematic
22 underestimation in the CTH occurrence frequencies in the LMS with respect to the
23 observations. The observations together with the model results demonstrate the importance of
24 isentropic, quasi-horizontal transport of water vapour from the sub-tropics and the potential
25 for the occurrence of cirrus clouds in the lowermost stratosphere and tropopause region.

1 **1 Introduction**

2 A large proportion of the uncertainties of climate change projections by general circulation
3 models (GCMs) arises from poorly understood and represented interactions and feedbacks
4 between dynamic, microphysical, and radiative processes affecting cirrus clouds (IPCC,
5 2014). Modelled climates are sensitive even to small changes in cirrus coverage or ice
6 microphysics (Kärcher and Spichtinger, 2010). Fusina et al. (2007) point out that the net
7 radiative impact strongly depends on ice water content, crystal number concentration, and size
8 distribution. Small changes in the effective radius of the size distributions can substantially
9 modify the surface temperatures.

10 Recent GCM studies (Sanderson et al., 2008, Mitchell et al. 2008) indicate that the climate
11 impact of cirrus clouds depends in particular on the fall speed of ice particles, which in turn
12 depends on ice nucleation rates (i.e. the concentrations of small ice crystals). The overall net
13 warming effect of cirrus clouds can be substantially reduced by changing the concentrations
14 of small ice crystals (i.e. the degree of bimodality) of the particle size distribution (PSD). The
15 size distribution strongly affects the representative PSD ice fall speed. Mitchell and Finnegan
16 (2009) investigated this sensitivity in more detail and concluded that cirrus clouds are a
17 logical candidate for climate modification efforts.

18 The large uncertainties in climate prediction caused by processes involving cirrus clouds
19 highlight the importance of more quantitative information on cirrus clouds by observations,
20 especially for optically thin and small particle cirrus clouds like contrails close to the
21 tropopause, which may have an overall cooling effect in contradiction to lower cirrus (Zhang
22 et al., 2005). However, uncertainties for the climate feedback of cirrus clouds are still very
23 large and a substantial reduction is needed (IPCC, 2014).

24 In particular, the altitude region of the Upper Troposphere and Lower Stratosphere (UTLS)
25 plays an important role. Changes and variability of UTLS composition are major drivers of
26 surface climate change. Even small changes of spatially highly variable concentrations of
27 water vapour (H₂O) have significant effects on the atmospheric radiation balance (e.g.
28 Solomon et al., 2010, Riese et al., 2012).

29 Detailed understanding and modelling of the transport pathways of water vapour, and
30 consequently the realistic representation of total water (gaseous and condensed form) in the
31 UTLS region are therefore crucial for the correct representation of clouds and water vapour in

1 climate models. Comprehensive analyses are published on transport processes from the
2 troposphere into the stratosphere and tracer proportions of the extra-tropical UTLS region
3 (e.g. Hegglin et al., 2009, Hoor et al., 2010, Ploeger et al., 2013). Rossby wave breaking
4 (Ploeger et al. 2013) and mid-latitude overshoot convection (Dessler, 2009) result in transport
5 and mixing of air masses into the extra-tropical UTLS on short time scales (weeks). On
6 seasonal time scales, downwelling by the deep Brewer-Dobson circulation branch moistens
7 the extra-tropical UTLS at altitudes above 450 K (Ploeger et al., 2013). Aged air masses
8 transported into the extra-tropical lower stratosphere from above are moistened by methane
9 oxidation in the upper and middle stratosphere and represent an important source for water
10 vapour in the middle stratosphere (e.g., Jones and Pyle, 1984, Rohs et al., 2006).

11 The imprint of various water vapour transport ways into the lowermost stratosphere on cirrus
12 formation has been investigated in a limited number of studies (Dessler, 2009, Montaux et al.
13 2010, Pan and Munchak, 2011, Wang and Dessler, 2012). The formation of cirrus clouds
14 above the mid-latitude tropopause is discussed so far quite controversially. Dessler (2009)
15 found relatively high occurrence rates of cirrus above the mid and high latitude tropopause in
16 space borne lidar data of the Cloud and Aerosol Lidar (CALIOP) instrument on the Cloud
17 Aerosol Lidar Infrared Pathfinder Satellite Observations (CALIPSO) (Winker et al., 2010).
18 The analysis of Dessler (2009) shows cloud top height occurrences above the tropopause of
19 up to 30-40% for mid-high and tropical latitudes and still 0.1% at 3 km or 40-50 K potential
20 temperature above the tropopause. Pan and Munchak (2011) (in the following abbreviated as
21 PM2011) showed that accurate tropopause definition and tropopause relative coordinates are
22 important for this type of analysis and reach significantly different conclusions based on the
23 same set of measurements. They find substantially fewer clouds above the tropopause than
24 Dessler (2009) and in their analysis the CALIOP data do not provide sufficient evidence of
25 significant presence of cirrus clouds above the mid-latitude tropopause. The remaining but
26 evidential events in the tropics show occurrences up to 24% in the western Pacific and are
27 usually located between the cold point and the lapse rate tropopause (up to 2.5 km above).
28 PM2011 speculated that most of these clouds are triggered by gravity wave induced
29 temperature disturbances, which typically are observed above deep convection areas (e.g.
30 Hoffmann and Alexander, 2010).

31 In contrast, cloud observations by mid-latitude lidar stations show frequent events at and
32 above the tropopause (e.g. Keckhut et al., 2005, Rolf, 2013). Many of them coincide with the

1 observations of a secondary tropopause (Noël and Haeffelin, 2007). Isentropic transport and
2 mixing of subtropical air masses with tropospheric high water values into the mid-latitude and
3 polar LMS may cause such events and Montaux et al. (2010), in a case study, were able to
4 reproduce the observation of such a cloud with an isentropic transport model by implementing
5 a simple microphysical cloud model. However in this study, the cloud was observed just at
6 the tropopause and not significantly above. Eixmann et al. (2010) investigated the dynamical
7 link between poleward Rossby wave breaking (RWB) events and the occurrence of upper
8 tropospheric cirrus clouds for lidar measurements above Kühlungsborn (54.1°N, 11.8°E). For
9 three similar cirrus events they found a strong link between low values of potential vorticity
10 (a proxy for RWB activity), enhanced up-draft velocities, and cloud ice water content. They
11 concluded that based on the climatology of poleward RWB events following the method of
12 Gabriel and Peters (2008) a parameterisation of the formation or occurrence of high and thin
13 cirrus clouds seems to be possible.

14 Although there are a couple of ground based lidar observations suggesting the presence of
15 cirrus clouds in the lowermost stratosphere (LMS), a region strongly influenced by isentropic
16 (quasi-horizontal) transport of air masses from the tropics (Gettelman et al., 2011), there are
17 open questions: Which microphysical process and specific meteorological conditions foster
18 the formation of ice particles in this specific region, how frequently do these cirrus clouds
19 occur on global scales, and are clouds tops or even complete clouds significantly above the
20 tropopause?

21 The currently most sensitive sensor in space for cirrus cloud observations is the CALIOP
22 lidar. Nonetheless, Davis et al. (2010) pointed out that the space lidar on CALIPSO might
23 miss 2/3 of thin cirrus clouds with vertical optical depth $\tau < 0.01$ in its current data products.
24 Clouds with such very low optically thicknesses have been observed by airborne lidars and in-
25 situ instruments in the validation campaigns for CALIPSO. Frequently these cloud layers
26 showed IWC values smaller than 10^{-5} g/m^3 (Davis et al., 2010) compared to the current IWC
27 detection limit in the CALIOP operational products of $1 - 4 \times 10^{-3} \text{ g/m}^3$ (Avery et al., 2012).

28 Here we argue that IR limb sounding from space provide an alternative measurement
29 technique of high sensitivity for the detection of optically thin clouds (Mergenthaler et al.,
30 1999, Spang et al., 2002, Massie et al., 2007, Griessbach et al., 2014), subvisible cirrus (SVC)
31 defined by the extinction range $2 \times 10^{-4} - 2 \times 10^{-2} \text{ km}^{-1}$ (Sassen et al. 1989), or the even
32 thinner ultra-thin tropical cirrus (UTTC) (Peter et al., 2003, Luo et al., 2003). The detection

1 sensitivity for clouds of IR limb sounders is in the range of spaceborne lidar measurements
2 (Höpfner et al., 2009, Spang et al., 2012). A 100 km or even 1 km horizontally extended
3 cirrus cloud is detectable by an IR limb sounder with an ice water content (IWC) of 3×10^{-6}
4 and $3 \times 10^{-4} \text{ g/m}^3$ respectively (Spang et al., 2012), presupposed that the cloud fills completely
5 the vertically field of view of the instrument. These values represent even better detection
6 sensitivity than the current CALIOP cloud products.

7 In this paper we present new analyses of measurements from the Cryogenic Infrared
8 Spectrometers and Telescopes for the Atmosphere (CRISTA) instrument during its 2nd Space
9 Shuttle mission in August 1997 (CRISTA-2) (Grossmann et al., 2002). Due to its unique
10 combination of moderate spectral resolution, high horizontal along track and cross track
11 sampling, and good vertical resolution and sampling, the CRISTA measurements are a unique
12 dataset for IR limb sounders in spite of information available from more modern satellite
13 missions today. A reanalysis of the dataset can add complementary information especially for
14 optically thin clouds compared to nadir passive and active instruments as well as limb
15 sounders in the uv-vis and microwave wavelength region. The characterisation of frequent
16 observations of northern hemisphere mid- and high-latitude cirrus clouds in respect to the
17 tropopause (above or below) are in the focus of the present study.

18 The paper is organised as follows. First we introduce the CRISTA instrument and the applied
19 data analysis methods followed by a section presenting the cloud top occurrence frequencies
20 (COF) in respect to the tropopause. The comparison of CRISTA water vapour and cloud
21 measurements presented in Section 4 suggests a strong influence of horizontal transport
22 processes of high water vapour values from the subtropics to the latitude of cloud formation.
23 A comparison with a global transport model can help to understand the origin and evolution
24 with time of the cloud observations around the tropopause. This is investigated in Section 5
25 with a Lagrangian transport model containing a simple cirrus parameterisation.

26

27 **2 Observations and analysis methods**

28 **2.1 CRISTA satellite instrument**

29 The Cryogenic Infrared Spectrometers and Telescopes for the Atmosphere (CRISTA)
30 instrument measured roughly one week in the UTLS during two space shuttle missions in

1 November 1994 and August 1997 (Offermann et al. 1999, Grossmann et al., 2002). The
2 measurements demonstrate the potential of the IR limb viewing technique to provide
3 information on several trace gas constituents (Riese et al. 1999a, 2002) and clouds (Spang et
4 al., 2002) with high spatial resolution. The spectral information in the wavelength (λ) region
5 4-15 μm is scanned with a resolution of $\lambda/\Delta\lambda \sim 500$, which is equivalent to 1.6 cm^{-1} at 830
6 cm^{-1} . The vertical field of view (resolution) is in the order of 1.5 km and a typical vertical
7 sampling of 2 km was used during CRISTA-2. A horizontal along-track sampling of 200 to
8 400 km was applied, depending on the measurement mode. An across-track sampling of ~ 600
9 km was achieved by using three telescopes for three viewing directions simultaneously. A
10 typical measurement net in the northern hemisphere is illustrated in Figure 1. Due to the
11 overlapping orbits and the 57° orbit inclination an even higher horizontal cross-track sampling
12 becomes obvious at high northern latitudes (~ 200 km for north of 60° latitude). The
13 spectrometers and optics were cryogenically cooled by helium to allow for measurements in
14 the middle and far infra-red (4–70 μm).

15 The instrument was hosted by the free-flyer system ASTRO-SPAS (Wattenbach and Moritz,
16 1997). The accuracy of the attitude system of the platform which was also used for two
17 astronomic missions is excellent. The final pointing accuracy in the limb direction for the
18 three viewing directions is in the order of 300 m (Riese et al., 1999a, Grossmann et al., 2002).
19 The effect of refraction through the atmosphere in the limb direction is considered in the
20 tangent height determination and can reduce the actual tangent height by up to ~ 300 m at 12
21 km altitude. This correction is crucial for the cloud top height determination in the next
22 section.

23 Here, we focus on the CRISTA-2 mission which took place from August 8 to 15 in 1997.
24 Details on the instrument, the mission, and the specific water vapour retrieval are given in
25 Grossmann et al. (2002), Offermann et al. (2002), and Schaeler et al. (2005) respectively. For
26 the water vapour retrieval the continuous spectral scans of the spectrometers allow the
27 selection of a spectral water vapour feature most suitable at tropopause altitudes (at a
28 wavelength of 12.7 μm). An onion peeling retrieval is applied to the CRISTA measurements
29 (Riese et al., 1999, Schaeler and Riese, 2001) and has the advantage of no upward
30 propagation of errors to altitudes levels above the optically thick cloud, even if the spectrum
31 is not removed from the retrieval. The contamination by the strong cloud emissions and
32 scattering processes in the corresponding IR spectra are too complex to model accurately in

1 the retrieval process, and these measurements are not taken into account in the water vapour
2 distributions presented later. The absolute accuracy of the water vapour retrieval is estimated
3 to be 22% (Offermann et al., 2002), though it is better at specific altitudes (10% at 215 hPa).
4 The precision is estimated to be 8–15% (Schaeler et al., 2005).

5 **2.2 CRISTA Cloud detection**

6 In the following special emphasis is put on cloud top height (CTH) observations at NH mid-
7 latitudes in respect to the tropopause, where isentropic horizontal transport of water vapour
8 from the subtropics to high latitudes may trigger cirrus formation in LMS. The cloud
9 detection for IR limb sounders has been investigated in detail over the last decade (Spang et
10 al., 2012, and references therein). For spectrally resolved measurements simple colour ratio
11 based methods are shown to be robust and accurate for the detection of cloudy spectra (e.g.
12 Spang et al. 2001, Sembhi et al., 2012). For the following analyses the cloud index (CI) is
13 defined by the colour ratio of the mean radiances from 788 to 796 cm^{-1} divided by the mean
14 radiances from 832 to 834 cm^{-1} , which was already applied to various airborne and
15 spaceborne limb IR instruments (e.g. Spang et al., 2002, 2004, 2007). The corresponding
16 CTH is the first tangent height where CI falls below the defined threshold value (CI_{thres}). The
17 left panel of Figure 2 illustrates a CI profile with the transition from clear sky conditions
18 ($8 > \text{CI} > 4.5$) to cloudy conditions ($\sim 4 > \text{CI} > 1.1$), where optically thick conditions are in line
19 with a CI-value of ~ 1.2 .

20 Various studies have shown that the detection sensitivity is linked to the detection threshold
21 and depends to some extent on the seasonal variation in the trace gas concentrations in the
22 applied spectral windows (e.g. Spang et al. 2012). The main limiting effect of the cloud index
23 method are high water vapour continuum emissions (for mixing ratios > 500 ppmv) in the mid
24 troposphere and below. Under such conditions a definite discrimination between clouds and
25 high water becomes difficult (Spang et al., 2004, 2007). Radiative transfer calculations show
26 that water vapour variations in the tropical tropopause region have only a marginal effect on
27 the numerator in the CI colour ratio and the corresponding CI-threshold approach (even a
28 factor of two reduction in water vapour, like observed at the tropical hygropause compared to
29 the higher stratospheric value causes only a $\Delta \text{CI}_{\text{max}} = 0.02$). The water vapour line emissions
30 are too weak to compete with dominating CO_2 and O_3 emissions in the 788-796 cm^{-1} region.

31

1 Spang et al. (2012) showed that limb IR measurements of cirrus clouds are most sensitive to
 2 the integrated surface area density along the limb path (area density path, ADP) and that ADP
 3 is a useful quantity for comparisons with global models or measurements in combination with
 4 radiative transport models. For example, the limb path can be traced through the 3D model
 5 output to generate the ADP quantity. ADP and CI show an excellent correlation and ADP can
 6 be retrieved from the measured CI values (Spang et al., 2012). For a homogeneous limb path
 7 segment ADP and limb ice water path (IWP) are related by the simple equation:

$$8 \quad ADP = 3 \cdot IWP / (R_{eff} \cdot \rho_{ice}) \quad (1)$$

9 with ρ_{ice} the mass density of ice, and R_{eff} the effective radius of the particle size distribution.
 10 More generally the limb IWP can be computed by the following relations, depending which
 11 parameters are known from the model or measurements:

$$12 \quad IWP = \int_0^{\infty} IWC \, dx = \int_0^{\infty} V \cdot \rho_{ice} \, dx = \frac{1}{3} \int_0^{\infty} A \cdot R_{eff} \cdot \rho_{ice} \, dx, \quad (2)$$

13 where R_{eff} and IWC are defined by the model, V and A represent volume and surface area
 14 density respectively (Spang et al., 2012). The authors retrieved a detection sensitivity in ADP
 15 for the cloud index approach in the order of $ADP_{thres} = 10^7 \mu m^2 \text{ cm}^{-2}$. If one assumes a typical
 16 effective radius for optically thin cirrus clouds of $10 \mu m$, this results in an equivalent limb
 17 IWP of 0.3 gm^{-2} .

18 Emissions by aerosol particles in the UTLS region can affect the CI values similar to clouds
 19 and a differentiation between ice and aerosol particles would be useful. Due to the very low
 20 volcanic activity after the major eruption of Pinatubo in 1991 for the rest of the 90s, the year
 21 of the CRISTA mission 1997 and the following years are a period of exceptional low UTLS
 22 aerosol load in the tropics (e.g. Vernier et al., 2011) and at mid-latitudes (SPARC, 2006). The
 23 long term records of measured aerosol extinctions by the satellite instruments SAGE II (at 0.5
 24 and $1 \mu m$) and HALOE (at $5 \mu m$) for 1997 show extremely low values for this period
 25 (SPARC, 2006). Radiative transfer model (RTM) calculations with extinctions transferred
 26 from the HALOE wavelength to the $12 \mu m$ region of CRISTA as well as for particle size
 27 distribution from balloon measurements at mid-latitudes (Deshler et al., 2003) have been
 28 performed to quantify the effect on the cloud index approach. The results show the aerosol
 29 equivalent CI values in the range of 4 to 6. A $CI < 3$ cannot be achieved for 1997 conditions
 30 (see also Spang et al., 2002). Consequently we can exclude that the detected events with

1 $CI_{\text{thres}}=3$ in the following analyses are related by radiance emissions of the background
2 aerosol or caused by an injection of volcanic aerosol in the tropics or mid-latitudes.

3 Further, for a more direct test we have applied to the data a new method for the differentiation
4 of sulphuric acid aerosol and ice particles developed for the MIPAS instrument by Griessbach
5 et al. (2013). The method uses additional wavelength regions at $\sim 960 \text{ cm}^{-1}$ and 1225 cm^{-1} to
6 provide an aerosol/ice classification. The different spectral slope of the continuum like
7 emissions for ice, H_2SO_4 , and volcanic ash makes the differentiation of these potential aerosol
8 and cloud types possible. If we apply the detection restriction of $CI < 3$ the new method shows
9 no aerosol but usually ice signals for most of the CRISTA spectra around the tropopause. This
10 analysis corroborates the conclusion derived above on the basis of RTM calculations that
11 values $CI < 3$ cannot be caused by stratospheric aerosol.

12 Cloud top heights detected with a cloud index threshold value of $CI_{\text{thres}}=3$ are presented in
13 Figure 1. Inhomogeneities in the measurement net are caused by special measurement modes,
14 where the free-flyer was pointed to specific regions of interest (e.g. the warm pool region over
15 Micronesia or validation sites). The dense horizontal coverage of the measurement net over
16 24 hours (here presented for August 9 to 10, 1997, noon to noon) allows to track the
17 horizontal transport patterns of trace gases for example streamers (e.g. Riese et al., 1999a,
18 2002) in conjunction with meteorological parameters like the potential vorticity (PV). Figure
19 1 shows PV contours for the 350 K isentrope. All meteorological data used in this study are
20 from the ERA Interim reanalysis dataset provided by the European centre for medium-range
21 weather forecasts (ECMWF) (Dee et al., 2011). The CTH distribution and PV contours suggests
22 a link between the dynamical features of horizontal transport processes like Rossby wave
23 breaking events (e.g. Juckes and McIntyre, 1987) and the presence of high cirrus clouds.
24 Contours of low PV (4 and 8 PVU, with $1 \text{ PVU} = 10^{-6} \text{ K m}^2 \text{ kg}^{-1} \text{ s}^{-1}$) are highlighting
25 elongated air masses from the subtropics to mid and high latitudes where coincidentally high
26 altitude clouds appear in the CRISTA observations.

27 High CTHs ($>12 \text{ km}$) are frequently present at mid ($40\text{-}60^\circ\text{N}$) and even at high geographic
28 latitudes ($>60^\circ\text{N}$) in regions of low PV. Nearly all of these high CTH locations show PV
29 values greater 2 PVU, a common threshold for the dynamical tropopause in the subtropics
30 (Holton et al., 1995), and marked in Fig. 2 by black circles. Whether these clouds are really
31 formed in the LMS and not just below the tropopause is a matter of particular interest in this
32 study. In addition, for exploring clouds in the vicinity of the tropopause it is important to

1 quantify accurately the uncertainties in cloud top and tropopause height. The following
2 sections will present more details on the analysis method and error estimates of both
3 parameters.

4 **2.3 Uncertainties in cloud top height determination**

5 The retrieved CTH from the CRISTA radiance profiles depends not only on the CI threshold
6 values but also critically on the vertical sampling of the instrument (typically 2 km during
7 CRISTA-2, see Figure 2) and the vertical size of the field of view (FOV) of the instrument.
8 The FOV of CRISTA is very well described by a Gaussian function with a full width half
9 maximum (FWHM) of 2.624 *arcmin*, which is equivalent to ~ 1.5 km at 15 km tangent height
10 (Offermann et al., 1999) and corresponds to a standard deviation of $\sigma_{\text{FOV}}=625$ m.

11 Uncertainties in the CTH are dominated by effects of the vertical FOV. If an optically thick
12 cloud is only filling the lower part of the FOV, the attributed CTH may overestimate the real
13 CTH. This potential error source was investigated in detail by modelled cloud index profiles
14 for various cloud conditions and background atmospheres (Figure 3). We calculated radiance
15 profiles of the analysed wavelength regions to compare the cloud index for varying cloud
16 altitude (6-20 km) and layer thickness (0.5 and 2 km), and extinction ε (10^{+1} to 10^{-4} km^{-1}).
17 Simulations were carried out with the line by line radiative transfer code RFM (Dudhia et al.,
18 2002). Scattering processes were neglected. For a full set of simulations a realistic parameter
19 space was chosen, i.e. CTHs between 6 and 16 km, different reference gas atmospheres, cloud
20 extinctions from 10^{+1} to 10^{-4} km^{-1} , and box type cloud layers with vertical extension of 0.5, 1,
21 and 2 km. The calculations were performed on a 100 m vertical grid. The pencil beam
22 radiance profiles were afterwards convolved with the FOV. By comparing the input CTH and
23 the simulated CTH we estimate the maximum error in CTH for multiple CI thresholds (grey
24 vertical lines in Figure 3). Four different threshold values (1.2, 2, 3, 4) have been investigated
25 for the various cloud layer extinctions and cloud vertical thickness. A detection threshold of 4
26 and 4.5 was applied for the Michelson Michelson Interferometer for Passive Atmospheric
27 Sounding (MIPAS) instrument (Fischer et al., 2008) in various studies for the detection of the
28 usually optically thin PSCs (e.g. Spang et al., 2003, Höpfner et al., 2005). Sembhi et al.
29 (2012) showed that CI_{thres} values up to 6 are acceptable for the MIPAS measurements
30 depending on the latitude and altitude region of interest.

1 Figure 3 shows the CI profiles of the pencil beam simulations and the CI profile with the FOV
 2 convolution for a homogeneous cloud layer for an optically thin ($\varepsilon = 3 \times 10^{-3} \text{ km}^{-1}$) cloud
 3 between 10 to 12 km (CTH = 12 km) and an optically thick ($\varepsilon = 10^{-1} \text{ km}^{-1}$) cloud between 11-
 4 13 km (CTH = 13km). The conservative threshold $\text{CI}_{\text{thres}}=1.2$ detects only optically thick
 5 clouds and consequently the CTH is underestimated due to the FOV effect. Optically thinner
 6 clouds are only detectable with a less stringent threshold ($\text{CI} > 1.8$, Spang et al., 2005a). The
 7 analysis for $\text{CI}_{\text{thres}}=2$ shows a maximum possible CTH error ($\Delta_{\text{max}2}$) of 0.6 km for all
 8 simulations. Higher thresholds result in higher detection sensitivity but cause higher
 9 uncertainties in CTH ($\Delta_{\text{max}3}=0.9$ km for $\text{CI}_{\text{thres}}=3$ and $\Delta_{\text{max}4}=1.4$ km for $\text{CI}_{\text{thres}}=4$) for optical
 10 thick clouds with $\varepsilon > 10^{-1} \text{ km}^{-1}$. Optically thinner clouds usually cause smaller maximum CTH
 11 errors.

12 However, the optically thin and thick example in Fig. 3 show that higher detection sensitivity
 13 will cause an overestimation of the CTH, in the examples for 0.8 and 1.25 km for $\text{CI}_{\text{thres}}=4$. In
 14 addition it should be noted that the actual CTH error of a measurement depends not only on
 15 CI_{thres} , but also on the relative distance of the measured tangent heights to the actual ‘real’
 16 cloud top (sampling). For CRISTA measurements the distances of the tangent point to the
 17 ‘real’ CTH in the atmosphere are statistically almost equally distributed with a maximum
 18 distance of ± 1 km due to the 2 km vertical sampling. The Δ_{max} values above are errors of a
 19 worst case scenario and represent the upper extreme of the FOV effect. Half of all detections
 20 of optically thick clouds will have a Δ_{CTH} smaller than $\Delta_{\text{max}}/2$, due to the fact that the FOV
 21 error for optical thick clouds declines linearly with declining difference between the sampled
 22 observation height and the ‘real’ CTH (see Figure 3).

23 In conclusion, the mean CTH error due to the FOV (for optical thick clouds) $\overline{\Delta_{\text{FOV}}}$ is
 24 consistent with $\Delta_{\text{max}}/2$. For optically thinner clouds Δ_{max} becomes systematically smaller (e.g.
 25 compare Figure 3a for thin and Figure 3b for thick conditions) and for the more stringent
 26 $\text{CI}_{\text{thres}}=2$ these clouds are only detectable at an observations height below the actually ‘true’
 27 CTH (negative CTH errors in Figure 3a). In the following analyses we used two thresholds,
 28 $\text{CI}_{\text{thres}}=2$ and $\text{CI}_{\text{thres}}=3$, for optimisation and best trade-off between quantified FOV effects and
 29 best detection sensitivity for optically thin clouds. The chosen CI values are equivalent to
 30 extinction coefficients of $\varepsilon > \sim 5 \times 10^{-3} \text{ km}^{-1}$ and $\varepsilon > \sim 2 \times 10^{-3} \text{ km}^{-1}$ respectively, and
 31 correspond to $\overline{\Delta_{\text{FOV}2}} = 250$ m and $\overline{\Delta_{\text{FOV}3}} = 450$ m.

1 It is certainly a strong overstatement to postulate optical thick conditions for all potential
2 cirrus cloud detections around the tropopause. How frequently cirrus clouds in the limb
3 appear as optical thick or thin, equivalent to large and small positive biases, is unknown and
4 therefore difficult to quantify. The slant ice water path (IWP), the IWC integrated along the
5 line of sight (Spang et al., 2012, and also section 2.2), determines the actual optical thickness
6 of the measured spectrum in the limb direction. Radiative transport model calculations for a
7 characteristic diversity of cirrus size distribution parameters (Griessbach et al., 2014) under
8 the assumption of vertically and horizontally homogeneous cloud layers show that the largest
9 FOV induced CTH errors Δ_{\max} (for $\varepsilon > 10^{-1} \text{ km}^{-1}$) can be generated from a cloud layer with
10 $\text{IWC} > \sim 3 \text{ ppmv}$ ($> 5 \times 10^{-4} \text{ g/m}^3$) (Spang et al., 2007, Fig. 5). This is a common value in IWC
11 in-situ measurements in the upper troposphere, typically close and or slightly greater than the
12 typical median values (Krämer et al., 2009) in the corresponding temperature range of the
13 CRISTA measurements. Consequently, it is very likely that the CRISTA statistics also
14 include a certain amount of underestimated CTHs by optically very thin clouds ($\text{IWC} \ll 3$
15 ppmv).

16 Uncertainties in CTH determination from broken cloud segments along the line of sight in
17 combination with the horizontal integration of the limb information and from the cross track
18 extension of the FOV (30 *arcmin*, $\sim 15 \text{ km}$) are not considered in the present analysis. Spang
19 et al. (2012) showed for the combination of realistic limb ray tracing through high resolved
20 2D IWC fields from ECMWF analyses and RTM calculation that due to the integrated view
21 of the limb sounder significant differences in the retrieved cloud top height are not expected
22 for two clouds with constant ADP. For example a large IWC concentrated over a short
23 horizontal distance or even multiple cloud fragments and a low IWC distributed
24 homogeneously over a large horizontal distance result in very similar vertical CI profiles and
25 corresponding CTHs. The study of Spang et al. (2012) showed that the size of the FOV and
26 the location of the CTH in the FOV are the driving factors for the CTH error. However, due to
27 the limb geometry cloud inhomogeneities along the line of sight can result in an
28 underestimation of the CTH with respect to the true CTH. If the cloud segment is placed
29 significantly in front or behind the tangent point ($> 150 \text{ km}$ for a FOV of 1.5 km) and
30 consequently at higher altitudes then the retrieved CTH will be negatively biased. This error
31 would therefore not explain the cloud observation above the tropopause.

1 **2.4 Radiosonde data**

2 In this study we used the radiosonde station composite data from the University of Wyoming,
3 Department of Atmospheric Science. For August 1997, a time period embedding the
4 complete CRISTA-2 mission, around 5000 radiosonde launches were available for coincident
5 comparison of tropopause location with respect to CTHs from CRISTA and for the global
6 validation of an improved tropopause determination with the ERA Interim dataset (section
7 2.5) at mid and high northern latitudes. Figure 2 illustrates a coincident radiosonde
8 temperature, relative humidity (RH) and ice saturation temperature profile in comparison to
9 the CRISTA cloud index profile. The cold point tropopause is clearly visible in the blue
10 temperature profile. The horizontal lines indicate the retrieved CTH from CI and lapse rate
11 tropopause based on coincident ERA Interim temperatures (details see section 2.5). Usually
12 radiosonde RH measurements around the tropopause have a low accuracy and act more like a
13 qualitative measure of humidity. Nevertheless, RH and the ice saturation temperature profile
14 indicate atmospheric conditions around the tropopause that allow for the existence of ice. This
15 is in coincidence with the slightly higher cloud layer detected by CRISTA, where CTH and
16 tropopause height (TPH) suggest a cloud above the local tropopause.

17 **2.5 Improved determination of the lapse rate tropopause for ERA Interim**

18 Accurate tropopause height determination is crucial for the location of cloud events with
19 respect to the tropopause as PM2011 already showed for the CALIPSO cloud detection. For
20 our analyses we used the ERA Interim reanalysis data on hybrid coordinates (Dee et al., 2011)
21 with original model resolution (60 levels and 600-1000 m resolution around the tropopause)
22 for the computation of the tropopause height. A three step approach is applied to the data. (1)
23 For each CRISTA tangent height the surrounding four ERA temperature and geopotential
24 height profiles are determined. Then the lapse rate tropopause was defined for each profile as
25 the lowest pressure (altitude) level at which the lapse rate is 2 K/km or less. The lapse rate
26 should not exceed this threshold for the next higher levels within 2 km (WMO, 1957). The
27 vertical resolution of the retrieved TPH cannot be better than the vertical grid resolution of the
28 temperature data and hence, can produce a significant positive bias for analyses with
29 tropopause related altitude coordinates (PM2011). In step (2) we applied a vertical spline
30 interpolation with 30 m vertical resolution to the temperature profile around the actual TPH of
31 step 1 and repeated the TPH computation with the artificially higher vertical resolution.

1 Finally, in step (3) the weighted mean with distance of the four surrounding grid points of the
2 observation point represents now the so-called high resolution tropopause height (TPH_{hr}). By
3 this approach of tropopause determination a more realistic lapse rate tropopause was found,
4 because the single TPH values are not attached to the altitude grid points of the analysis data
5 anymore.

6 Comparisons with radiosonde data set for August 1997 show a good correspondence between
7 the TPH_{hr} and the lapse rate tropopause of the radiosonde for the coincidences with CRISTA
8 profiles (see also Figure 2). A statistical analysis of the difference in TPH between 5304
9 sonde profiles in the latitude range $30^{\circ}N$ and $80^{\circ}N$ and the ERA Interim based TPH_{hr} for
10 August 1997 showed a mean difference of 15 m and a standard deviation of 650 m. The latter
11 value is exactly the same value as found in the analysis of PM2011 for a comparison between
12 radiosonde and National Center of Environmental Prediction Global Forecast System (GFS)
13 data for a June-July-August season in 2007. The good correspondence gives us confidence
14 that the described TPH_{hr} is the best possible and reliable approach for a tropopause
15 determination for each CRISTA profile. In addition, the standard deviation of the differences
16 appears to be a realistic estimate for the uncertainty of TPH_{hr} .

17

18 **3 CRISTA cloud top height occurrence with respect to the tropopause**

19 **3.1 Tropopause derived from radiosonde data**

20 A comparison of tropopause heights determined from radiosonde measurements with the
21 detected CTHs in the tropopause region allows a first quantitative assessment of the
22 indication for frequent observation of optically thin clouds by CRISTA in the LMS like
23 illustrated in Figure 1. A miss time of two hours and miss distance of 200 km coincidence
24 criteria were chosen to minimise uncertainties in the comparison. For 158 CTH detections
25 close to the tropopause and north of $40^{\circ}N$ (with $CI_{thres}=3$, $CTH-TPH > -500$ m, and TPH
26 defined from co-located ERA Interim temperatures) we found 188 coincident radiosonde
27 profiles. The tropopause of 62 radiosonde profiles (~33%) is pinpointed more than 500 m
28 below the coincident CTH of CRISTA. This indicates a remarkable fraction of clouds well
29 above the tropopause and emphasizes the question if these high altitude clouds in the LMS are
30 a common feature or a rare incidence. However, the only limited number of good

1 coincidences between CRISTA and radiosonde measurements with respect to adequate miss
2 time and distance criteria allows no profound conclusions on this question. A statistical
3 analysis of all cloud observed in the tropopause region together with the collocated
4 tropopause heights based on ERA Interim may solve this problem.

5 **3.2 Statistical analysis with tropopause derived from ERA Interim**

6 For the statistical analysis of cloud occurrences around the tropopause we choose a vertical
7 coordinate independent of the temporal and spatial location of the tropopause. Therefore
8 thermal tropopause relative coordinates are applied in the following similar to PM2011. These
9 coordinates are used extensively in chemical tracer analyses (e.g. Tuck et al., 1997, Pan et al.
10 2007, Kunz et al., 2013) and temperature profile analyses (e.g. Birner et al., 2006). The actual
11 distance of a detected CTH to the tropopause is defined by $\Delta_{CTH} = CTH_i - TPH_i$ where the
12 index i is attributed to an individual measurement profile. For displaying results it is often
13 more helpful to adjust the reference altitude to the mean tropopause height (TPH_{mean}). The
14 tropopause related altitude Z_r is then defined by:

$$15 \quad Z_r = \bar{Z}_{trop} + (Z - Z_{trop}) , \quad (3)$$

16 with Z the observations altitude or the CTH, Z_{trop} the individual tropopause, and \bar{Z}_{trop} for
17 example a daily or monthly zonal mean tropopause. Here we use for \bar{Z}_{trop} the zonal mean
18 tropopause during the CRISTA-2 measurement period. Figure 4 presents the results of CTH
19 height occurrence frequencies (COF) in respect to the single profile tropopause location
20 defined by the approach above and a vertical grid size of 0.5 km. Latitude bands covering the
21 whole northern hemisphere observations by CRISTA have been defined for the tropical (0-
22 20°N), subtropical (20-40°N), mid (40-60°N) and high latitudes (60-75°N). The vertical
23 distributions are very different for the various latitude bands. A joint feature is the location of
24 the maximum in COF in a layer 0.75 to 1.25 km below the tropopause for almost all latitude
25 bands. In parts this is caused by the limb geometry. The probability to detect a cloud along the
26 line of sight located above the actual tangent height is enhanced with penetrating deeper into
27 the troposphere. This effect causes artificially overestimated COFs below the real maximum
28 in the COF distribution and is especially a large bias in the tropics, where horizontally small
29 extended and patchy distributed cloud systems (<50 km), e.g. by deep convection events, are

1 generating unrealistic high COFs in limb observations (Kent et al., 1997, Spang et al., 2012).
2 Note that CTHs assigned to such observations are actually low biased.

3 Only the subtropics show the COF maximum at slightly lower altitudes. But more
4 remarkable, generally very low COF values are found around the tropopause compared to the
5 three other latitude bands. This local minimum at 20-40° latitude in cloud probability has
6 been already observed in various limb sounder observations around the tropopause (e.g. Wang
7 et al., 1996, Spang et al., 2002, Spang et al. 2012).

8 Figure 4 presents the COF values for both CI threshold values. The frequencies for $CI_{\text{thres}}=3$
9 are systematically higher than for the less sensitive threshold $CI_{\text{thres}}=2$, and more clouds are
10 detected well above the predefined tropopause and also above the maximum in the COF
11 distribution. For the more sensitive detection method $CI_{\text{thres}}=3$ a COF of 3% and 4% (217
12 events in total) is found in the altitude grid box 500-1000 m for mid- and high-latitudes
13 respectively. Even in the 1000-1500 m grid box above the tropopause COFs of ~1% are
14 observed in both latitude bands (59 events). These COF values above the tropopause indicate
15 significantly larger occurrence rates than found in ground based lidar observations (e.g. Noel
16 and Haeffelin, 2007, Rolf, 2013). The typically observed frequencies of 4-10% of cross
17 tropopause cirrus were referred to the total number of lidar profiles with cirrus clouds and not
18 to the total number of observations (cloudy and non-cloudy) such for the satellite data. An
19 equivalent approach would result in significantly smaller COF values for the lidar
20 measurements.

21 In addition, the tropics show a pronounced local maximum well above the tropopause for
22 $CI_{\text{thres}}=3$. The 100 m running mean statistic of 500 m grid boxes (red symbols) indicates that
23 the feature is not a sampling artefact caused by an interplay of the measurement altitudes with
24 the vertical gridding of the COF analysis.

25 Exceptional events like wildfires with pyro-convection are potential sources for unexpected
26 enhanced UTLS aerosol load (e.g. Fromm et al., 2010) and may cause the unexpected
27 secondary maximum above tropical tropopause in the CRISTA COF results. High fire
28 activity was observed in the time frame of the CRISTA mission and the following months
29 over Borneo caused by the strong 1997/8 El Nino (e.g. Wooster et al. 2012). We checked the
30 longitudinal distribution for the tropical CTH events above the tropopause, but found no
31 specific clustering of these events above the Borneo region. In contrast, the observed regions

1 are inline with the typical regions for high subvisual cirrus cloud occurrence in the tropical
2 tropopause region (e.g. Wang et al., 1996). For summer conditions these are the warm tropical
3 landmasses and the Micronesia area – the so-called warm pool region. Due to the specific El
4 Nino conditions the latter region was extended in direction to the mid pacific (e.g. Spang et
5 al., 2002) which is also observed in the CRISTA cloud distribution above the tropopause. The
6 tropical secondary maximum is so far not observed by other sensors. Based on the data
7 investigated here, we cannot decide whether the occurrence of subvisual cirrus well above the
8 tropopause is a regular feature or a particular event in the time frame of the CRISTA mission.

9 **3.3 Statistical tests of cloud top occurrence distribution**

10 We have investigated in detail how the measurement uncertainties of the tangent point
11 altitude, tropopause height, and cloud top height (section 2) might influence or even falsify
12 the COF statistics. Where TPH and tangent altitude errors are well described by a Gaussian
13 distribution (with corresponding standard deviations), the CTH error (Δ_{CTH}) caused by the
14 vertical FOV effect for optically thick clouds acts like a positive bias in the cloud top height
15 determination.

16 Monte Carlo (MC) simulations with the CRISTA measurement ensemble of cloudy and non-
17 cloudy profiles have been performed taken into account (a) statistical and (b) systematic error
18 sources. For both types of simulations all CTHs above the tropopause were excluded from the
19 dataset and the remaining CTH observations have been modified by a randomly distributed
20 statistical uncertainty or a systematic positive offset value with a Gaussian amplitude. The
21 results show that statistical (noise) errors like the TPH uncertainty with $\sigma_{\text{TPH}} = 650$ m or even
22 an overestimated value of 1000 m cannot reproduce the measured vertical COF distribution
23 and cannot create the relative large COFs observed above the tropopause.

24 For testing the systematic errors we applied to all CTH observations below the tropopause a
25 FOV-like, Gaussian-shaped, and only positive offset distribution. This approach is equivalent
26 to the assumption that all clouds below the tropopause are optically thick (upper limit), are
27 creating a positive offset, and are detected with the randomly distributed observation heights
28 of CRISTA. The results for $|\sigma_{\text{FOV}}| = 750$ m, a larger value than the real CRISTA $\sigma_{\text{FOV}}=625$ m,
29 show comparable COF distributions for mid and high latitudes and can create similar COF
30 values above tropopause to the original statistic. Larger $|\sigma_{\text{FOV}}|$ produces overestimated COF
31 values well above the tropopause (>1.5 km), significant underestimates below the tropopause,

1 and can be excluded. Surprisingly, the MC simulations were not able to reproduce the tropical
2 COF distribution with the positive bias approach. These two negative tests, large $|\sigma_{\text{FOV}}|$ and
3 irreproducible tropical COF distribution, are additional constraints for a systematic and large
4 FOV effect above the tropopause. In addition it is very unlikely that all clouds around the
5 tropopause are optically thick (only <50%, see section 2.3). Consequently it is very unlikely
6 that this type of cloud is responsible for an artificial enhancement in COF above the
7 tropopause like observed by CRISTA in Figure 4.

8 An additional and substantial argument against a large systematic FOV effect is the different
9 behaviour between tropical and mid/high latitudes in the measurements compared to the
10 simulations. A positive bias for optically thick clouds should modify the pronounced
11 maximum peak 1 km below tropical tropopause in the following way and is confirmed in the
12 MC simulations: the observations would show a broader distribution and a significant extent
13 of enhanced COF values in direction to higher altitudes similar to the mid and high latitudes.
14 But this behaviour is not observed in the tropical measurements (Figure 4a). A shift to higher
15 altitudes can be reproduced in the error simulations with $|\sigma_{\text{FOV}}| = 750$ m, but contrariwise it is
16 creating strong enhanced COFs just below tropopause and reduced values below. The overall
17 effect in the simulations, a positive shift of the whole distribution, is not observed in the
18 original data.

19 In conclusion, taken all uncertainties into account the CRISTA COF distribution indicates a
20 significant amount of cirrus cloud observations in the lowermost stratosphere. To our
21 knowledge this is the first time such findings are reported for space-borne limb
22 measurements.

23 **3.4 Comparison with SAGE I**

24 The Stratospheric Aerosol and Gas Experiment II (SAGE II) instrument is a limb sounder
25 with a vertical resolution and sampling of 0.5 km (e.g. Wang et al., 1996). The solar
26 occultation technique allows only measurements of ~30 profiles per day and consequently
27 significantly larger time periods than for CRISTA are necessary for comparison on global
28 cloud global statistics. First comparisons between CRISTA cloud observations and subvisual
29 cirrus cloud statistics retrieved from SAGE (Wang et al., 1996) have been presented in Spang
30 et al. (2002). CRISTA showed slightly smaller cloud occurrence frequencies in the tropopause
31 region than SAGE II. In the analyses a CI_{thres} of 2 was applied to the data, which missed

1 optically thinner clouds in the CRISTA measurements (about 2-5% more CTHs are observed
2 in the LMS for $CI_{\text{thres}}=3$ instead of $CI_{\text{thres}}=2$ at a certain altitude bin, Figure 4). For summer
3 1997 (June, July, August) the zonal mean occurrence frequencies of SAGE II showed
4 occurrence frequencies up to 10-15% above the mid-latitude mean tropopause. This is inline
5 with analyses by Wang et al. (1996) for the SAGE II 1985-1990 climatology; monthly time
6 series and multi-annual means (Plate 6, Fig. 3) show similar values above the tropopause.
7 These frequencies are even larger than the COFs in the actual CRISTA analyses (maximum
8 10%). However, a quantitative comparison of both analyses is difficult. Here, we present
9 CTH occurrence frequencies instead of cloud occurrence frequencies, where cloud detections
10 below the CTH are considered as well and result in higher occurrence frequencies. In
11 addition, the former analyses have not considered tropopause related coordinates (section 3.2)
12 which may cause a systematic overestimation in occurrence frequencies above the tropopause.

13 **3.5 Comparison with ice supersaturation measurements**

14 The existence of ice supersaturated regions (ISSR) is a precondition for the formation of
15 cirrus clouds. ISSRs have similar vertical and horizontal scales and occurrence distribution
16 like SVC (e.g. Gierens et al., 1999, Spichtinger et al., 2003a), and are observed with various
17 ground, air, and space-borne sensors. Statistics in respect to the tropopause location are less
18 frequently reported. Spichtinger et al. (2003a) showed for 6.2% of the regular balloon
19 launches over Lindenberg, Germany (52.22°N, 14.12°E), ISSRs in the lowermost
20 stratosphere. This amount fits well to the COFs observed by CRISTA at mid-latitudes. But
21 taken into account that larger supersaturations than 100% are necessary for homogeneous
22 freezing of ice (Koop et al., 2000) then the observed ISSR occurrence seems still too low to
23 explain the large COFs by CRISTA.

24 Satellite observation of ISSR should allow a better comparison with the CRISTA COF results.
25 Spichtinger et al. (2003b) showed for satellite based ISSR measurements with the Microwave
26 Limb Sounder (MLS) instrument very low occurrence frequencies in the mid-latitude
27 tropopause region (maximum 2-3 % at 215 hPa). The limited vertical resolution (~3 km) of
28 MLS and integration along the line of sight (~ 200 km) will reduce the detection sensitivity
29 for ISSR by factor of 0.2 compared to data from the Measurements of Ozone and water
30 vapour in Airbus In-service aircraft experiment (MOZAIC). Gierens et al. (2000) found that
31 the MOZAIC flights from 1995-1997 were about 15% of their time in ice supersaturated air

1 masses. Stratospheric ISSR events were only rarely found in the MLS data, but only a crude
2 tropopause determination was applied in the analyses and may create biases in the results
3 (Spichtinger et al., 2003b). More recent analyses use MOZAIC data in combination with
4 Atmospheric Infrared Sounder (AIRS) specific humidity and clouds data to estimate
5 occurrence frequencies of ice supersaturation (Lamquin et al., 2012). The authors find
6 significant larger frequencies than in the MLS analysis in the mid-latitude tropopause region
7 (20-30%) and indication for ISSR occurrence of 10-20% at the mid-latitude zonal mean
8 tropopause and above (Fig. 11). These numbers would favour more frequent formation of
9 cirrus clouds in the LMS.

10 **3.6 Comparison with ground based lidar measurements**

11 There are a couple of recent studies on the properties of cirrus clouds at mid-latitudes based
12 on ground based lidar observations (Dupont et al., 2010, Hoareau et al., 2013, Dionisi et al.,
13 2013). The analyses show a significant and large proportion of optically thin cirrus clouds in
14 the upper troposphere (42% of all profiles, Hoareau et al, 2013), in the tropopause region
15 (30% of all and 9% of the cloudy profiles, Dionisi et al., 2013) or even more precisely
16 localised above the tropopause (up 10% of all cloudy profiles, Rolf, 2013). However there is
17 only one study by Noel and Haeffelin (2007) of a longer time series with detailed cirrus
18 analysis with respect to the tropopause. Measurements were provided by a lidar system
19 located at the Site Instrumental de Recherche par Télédétection Atmosphérique (SIRTA)
20 observatory (48.71°N, 2.21°E). Tropopause characteristics are determined by a nearby
21 radiosonde station. Between 2002 and 2006 the cloud measurements show 5% cross-
22 tropopause cirrus (cloud base below and top above the tropopause) and 2% inter-tropopause
23 (cloud base above tropopause) events. In total, 2.5% of all observations (cloudy and non-
24 cloudy profiles) show cloud tops above the tropopause, a significant smaller number than the
25 integrated above-tropopause COFs of ~10% for mid-latitudes found in the CRISTA data (Fig.
26 4) but very similar to the COF value of 3% for cloud events significantly above the
27 tropopause ($CTH - TPH > 0.5$ km).

28 **3.7 Comparison with the CALIPSO lidar**

29 For a brief comparison with the CALIOP lidar on CALIPSO results from PM2011 are
30 superimposed in Figure 4 for tropical and mid-latitude observations. For mid-latitudes

1 CRISTA and CALIOP show very similar results at the tropopause and even though the time
2 period and observations geometry are rather different (7 day mean in August 1997 from limb
3 measurements versus multi annual seasonal mean June 2008 to May 2010 from nadir
4 measurements). In this region even the absolute COF values are in close agreement. However,
5 in the grid boxes 500-1000 m and 1000-1500 m above the tropopause CRISTA detected ~2
6 times more clouds than CALIPSO. Below the tropopause the limb sounder statistic shows a
7 substantial larger maximum in COF. This is primarily due to the long limb path integration
8 and the artificially enhanced number of cloud detections well below the tropopause by higher
9 altitude cloud fragments along the line of sight, and only secondary due to the better detection
10 sensitivity for horizontally extended clouds in the limb compared to the short nadir viewing
11 direction.

12 The tropical distribution looks more different, especially below the tropopause, where again
13 the overestimation due the limb geometry plays a role. At the tropopause (+/- 500 m), where
14 this effect is negligible, both instruments show similar COFs. Well above the tropopause (500
15 to 1500 m) CRISTA COFs are again significantly larger than CALIPSO and indicate the
16 presence of optically very thin clouds, which are currently not detected in the CALIPSO data
17 products (see also section 1). It should be noted that the CALIOP instrument may have
18 observed these clouds, but the current detection threshold of the operational data products is
19 not capable to detect ultra thin cirrus clouds. This was already shown by Davis et al. (2011) in
20 a validation study with airborne lidar and in situ particle measurements. Modified detection
21 schemes with larger horizontal averaging of the high resolution Level 1 profile data of
22 CALIOP (e.g. 30 or 50 km instead of currently 5 km) may substantially improve the detection
23 sensitivity for ultra thin cirrus clouds (M. Vaughan, personal communication). The current
24 detection limit for cirrus clouds averaged horizontally to 5 km for the 532 nm backscatter
25 channel result in a retrieved extinction value of 0.005 to 0.02 km⁻¹ (Avery et al., 2012), which
26 represents an equivalent IWC of 0.1 to 4 x 10⁻³ g/m³.

27 However, the IR limb sounder detection limit can be considerably better depending on the
28 horizontal extent of the cloud and depending how much of the vertical field of view is
29 covered by the cloud. The ADP_{thres} of 10⁷ μm/cm² (section 2.2) is equivalent to an IWC of
30 10⁻⁶ g/m³ for a cloud layer with 100 km horizontal times 1.5 km vertical extent (by assuming
31 a constant R_{eff} of 10 μm for the ice particles, see Eq. 1 and 2). This is about two order of
32 magnitude better than the current CALIOP product. A thinner cloud layer will almost linearly

1 enhance the detection threshold, depending on where the cloud layer is placed in the FOV of
2 CRISTA. Consequently a cloud fragment of 3 km horizontal times 0.5 km vertical extent is
3 still detectable by the CRISTA instrument if the cloud contains a mean IWC $> 10^{-4} \text{ g/m}^3$, a
4 value in the size or even smaller than the current IWC detection limit of CALIOP.

5

6 **4 Horizontal distribution of water vapour and clouds in the UTLS**

7 **4.1 Cloud top height distributions**

8 Four days during CRISTA-2 have a measurement net dense enough for hemispheric analyses
9 of horizontal structures in cloud and trace gas distributions. Figure 5 presents the daily cloud
10 top height distribution detected with the algorithms described in section 2.2 for August 10 to
11 13 at midnight ± 12 hours. Potential temperature (Θ) has been used as vertical coordinate and
12 CTHs in km are converted to Θ by coincident ERA Interim temperature and geopotential
13 height information. Only clouds detected in the altitude range 330 to 370 K are presented, an
14 atmospheric layer usually located in the lower half of the lowermost stratosphere (LMS) at
15 mid and high latitudes, and clearly in the upper troposphere and tropopause region for the
16 tropics and subtropics.

17 The observations show frequent high cloud top Θ (Θ_{CTH}) events in regions where elongated
18 PV contours as well as horizontal winds (not shown) are suggesting strong horizontal
19 transport and mixing processes extending from mid-latitudes ($\sim 40^\circ\text{N}$) to high northern
20 latitudes. Main regions are over the eastern Pacific with extension in direction to Alaska, the
21 north-eastern US directed to Greenland, from North-Atlantic and Central-Europe towards
22 northern Scandinavia and the Baltic region, and from China towards Siberia. High altitude
23 clouds are observed up to the northern edge of the CRISTA measurements at 74°N (e.g. over
24 northern Scandinavia and the Baltic Sea on August 10). During the four days of observations
25 the frequency for high Θ_{CTH} ($> 350\text{K}$) events north of the subtropical jet region seems to
26 decline.

27 The highest detected Θ_{CTH} (350-360 K) are in most cases above the local tropopause
28 indicating an origin of the detected cloudy air masses in the LMS. CTHs below 350 K in
29 regions dominated by high CTHs (e.g. in the Scandinavia-Baltic-Sea streamer) may be caused
30 by a 'real' lower altitude tropospheric cloud, but can also indicate underestimated CTHs

1 caused by the vertical sampling of the CRISTA measurements. The constant 2 km vertical
2 step size during CRISTA-2 in combination with a slightly drifting top altitude from one
3 profile to the next with time and latitude result in significant differences in the absolute
4 tangent height between even subsequent orbits (up to 1 km) with close geographical co-
5 location. Consequently a large cloud structure with nearly constant CTH may be detected at
6 different altitudes in two subsequent orbits at higher latitudes or in the tropics on up and down
7 leg of a single orbit.

8 **4.2 Water vapour measurements during CRISTA-2**

9 The horizontal distribution of the CRISTA water vapour at the 350 K isentrope is illustrated
10 in Figure 6 for the same days like in Figure 5. For better visualisation the data of individual
11 CRISTA H₂O profiles have been first interpolated to a constant theta level (here 350 K).
12 Vertical interpolation around the tropopause and below take always the risk that it may create
13 some numerical diffusion and artificially enhanced water vapour mixing ratios at the grid
14 level due to the strong exponential gradient in the mixing ratio profile below the tropopause.
15 This effect was minimized by logarithmic interpolation. In a second step a horizontal
16 interpolation on a regular grid (1°x1°) was performed by means of distance-weighted
17 averaging. Data gaps in the tropics are mostly due to clouds.

18 The CRISTA water vapour measurements were validated with the Microwave Limb Sounder
19 (MLS) and airborne in situ instruments (Offermann et al, 2002). The comparisons showed
20 good agreement in the coincidence statistics and a retrieval accuracy of 10% was estimated
21 for the data. The precision of the data is 8% for values >10 ppmv, and 8–15% for smaller
22 values (Schaeler et al., 2005). Consequently, the horizontal structures in Figure 6 are reliable.

23 Transport of water vapour from the tropical troposphere into the LMS on the 350 K isentropic
24 surface seems evidential in Figure 6. Shown are water vapour values as observed by
25 CRISTA-2 on August 10 to 13 at midnight ±12 hours. Rossby wave breaking events result in
26 an erosion of the tropopause that can be identified by the cut-off of PV and water vapour
27 contour lines over the Atlantic to Scandinavia and the Baltic sea, over the east northern
28 pacific in the direction of Alaska or from the eastern US in the direction of Greenland. The
29 intense wave processes are accompanied by fast isentropic transport of water vapour deep into
30 the LMS. These horizontal structures of high water vapour are nearly coincide with the
31 ‘unusual’ high CTH observation shown in Figure 5.

1 The water vapour values do not include the locations of optically thicker cloud observations,
2 because a corresponding filter ($CI < 2$) was applied before the retrieval. However, it is evident
3 that cloudy areas are embedded in regions of relatively high water vapour values. More
4 quantitative analyses exclusively from the satellite observations are difficult, because for most
5 cloudy CRISTA observations no adequate water retrieval is available.

6

7 **5 Comparison with the CLaMS model**

8 **5.1 The CLaMS model**

9 The Chemical Lagrangian Model of the Stratosphere (McKenna et al. 2002a, 2002b, Konopka
10 et al. 2007) is a chemistry transport model based on three-dimensional forward trajectories,
11 describing the motion of air parcels. Additional to advection by winds, irreversible small-
12 scale mixing between air parcels induced by deformation of the large scale flow is considered
13 in the model (McKenna et al., 2002a, Konopka et al. 2004). The mixing intensity is controlled
14 by the local Lyapunov coefficient of the flow, thus leading to stronger mixing in regions of
15 large flow deformations. The sensitivity of simulated UTLS water vapour on the intensity of
16 this quantity is discussed by Riese et al. (2012). The model uses a hybrid of pressure and
17 potential temperature as vertical coordinate system first proposed by Mahowald et al. (2002).

18 **5.2 Model setup**

19 The CLaMS simulation was started in mid May 1997, three months in advance of the
20 CRISTA observations, to give the model enough time for spin-up. The model was driven by
21 six hourly ERA Interim re-analyses with a mixing time step of 24 hours. The calculation of
22 water vapour in CLaMS includes a simplified dehydration scheme, similar to that applied in
23 von Hobe et al. (2011). Gas phase water in CLaMS is initialized at the beginning of the
24 simulation utilizing the specific humidity taken from ERA Interim data. Boundaries are
25 updated every CLaMS step from ERA Interim data as well. The lower boundary for this run is
26 at 250 K with respect to the hybrid vertical coordinate, corresponding to approximately 500
27 hPa.

28 The formation of ice is parameterised either by using a fixed value of 100% for saturation
29 over ice (a value commonly used) or by a temperature dependent parameterisation for

1 heterogeneous freezing (Krämer et al., 2009). The latter method was finally used in the model
2 simulations presented below. This parameterisation results in saturation values between 120%
3 and 140% for the temperature range from 180 K to 230 K. Water vapour with values above
4 these saturation levels is removed from gas phase and added to the ice water content. Water
5 vapour and ice water content are transported and mixed like any other tracer or chemical
6 species. Evaporation at 100 % saturation and sedimentation of ice by assuming a uniform
7 particle density and size distribution (Krämer et al., 2009) as well as parameterised processes
8 like re- and de-hydration are considered, with the only exception of re-hydration by formerly
9 sedimented particles. For sedimentation the terminal settling velocity is calculated. The
10 corresponding sedimentation length is compared with a characteristic height defined by the
11 vertical resolution of the model around the tropopause (~ 650 m for this simulation), and the
12 related fraction of ice is removed. This mechanism was successfully used for long term
13 studies with CLaMS (Ploeger et al. 2011, Ploeger et al. 2013). The horizontal resolution of
14 the simulations is in the range of 70 km.

15 **5.3 IWC and water vapour distribution in the model**

16 In a first step we investigated CLaMS model results for water vapour and ice water content on
17 synoptic maps of isentropic surfaces like in Figure 7. Afterwards model output is analysed by
18 applying the instrument specific limb geometry to the data, which is described in the next
19 subsection.

20 In the examples of Figure 7 isentropic surfaces of $\Theta=350$ K are selected, which represent a
21 nearly constant geometrical height with changing latitude, where isentropical transport can
22 cross from the tropical UT into the mid-latitude LS. In Figure 7 both IWC and water vapour
23 show distinctive streamer structures on two successive days (August 9 and 10). The streamers
24 are elongated and spread out to mid and high northern latitudes. Especially the water vapour
25 distribution suggests that regions of high water vapour are peeled off from the subtropical jet
26 region, as typically observed in PV fields during Rossby wave breaking events (e.g. Homeyer
27 and Bowman, 2013). These sub-tropical air masses are transported to and mixed in at high
28 latitudes, where under favourable conditions the formation of cirrus clouds might be possible.
29 Fine structures of water vapour and IWC can be observed similar to and more fine structured
30 than the superimposed PV contours. The IWC structures are less pronounced and indicate

1 significant less cloud formation at mid and high latitudes in contrast to the CRISTA
2 observations (Figure 5).

3 **5.4 How to compare global model data and limb measurements?**

4 For a quantitative comparison between the model data and limb measurements it is crucial to
5 take into account the observation geometry and to apply averaging kernels of the instrument
6 to the model data. In an optimised but very expensive process current investigations simulate
7 the original measurement quantity of the instrument (e.g. here IR radiances) by a specific
8 instrument simulator based on 3D input parameter of a climate chemistry model (e.g. Bodas-
9 Sacedo et al., 2011). This approach will reduce the uncertainties usually introduced by the
10 complex retrieval process of the instrument target parameter (e.g. IWC, specific humidity or
11 other trace gases) and is used for the validation of climate models. The detailed consideration
12 of the observation geometry is especially important for comparisons with cloud measurements
13 in the limb (e.g. Spang et al., 2012). Therefore we applied several processing steps for better
14 representation of two major instrument-specific effects of the CRISTA measurements.

15 In the first step, the temporal offsets between the asynoptic measurement times of the satellite
16 and the synoptic time steps in the model output (every 24 hours) have been compensated. For
17 this purpose backward trajectories of all CRISTA observations below 25 km to the next
18 synoptic model output time, usually every 24 hours at 12:00 were computed. Starting from
19 these synoptic locations the cirrus module of CLaMS was run forward in time to the asynoptic
20 time of the individual CRISTA observation. By this approach the formation and evaporation
21 of ice clouds in a time frame of maximum 24 hours between model output (12:00) and
22 observation is taken into account.

23 Secondly, we implemented an integration of the signal along the line of sight. A limb ray
24 tracing from the original position of the CRISTA satellite to the tangent point and the follow-
25 on to deep space has been applied to sample the model data. In case of CRISTA the tangent
26 height layer for the 1.5 km FOV has an extension of ~280 km. Deeper tropospheric
27 observations result in a factor of 2-3 longer (e.g. in the tropics) effective path lengths through
28 the atmosphere where a cloud can occur. In the tropics for a tangent height at 10 km the
29 maximum potential cloud occurrence altitude extents up to a height of ~18 km and a
30 corresponding line of sight segment of ~640 km should be considered in the limb ray tracing.

1 Finally we have used the simulated IWC to compute the IWP for a CRISTA-like cloud
2 detection in the CLaMS model fields. A 30 km step width along the line of sight over a
3 distance of +/- 1000 km with respect to the tangent point has been chosen, which is in line
4 with the horizontal resolution of the model. Then IWC_{CLaMS} has been interpolated on the line
5 of sight grid locations. A CTH detection is defined when the first (top) line of sight beam of a
6 CRISTA profile shows an $IWP_{CLaMS} > 0$. The latter fact is neglecting any detection sensitivity
7 threshold of the instrument and represents therefore an upper limit of what a CRISTA-like
8 instrument would detect in the cloudy atmosphere modelled by CLaMS.

9 An example of the CRISTA-like limb IWP is given in Figure 8. All tangent heights between
10 the 330 and 370 K isentrope with $IWP > 0$ are presented for 1997 August 10 00:00 +/- 12
11 hours. The results can be compared with Figure 1 and Figure 5a, even though these figures
12 show the CTH of a measured profile. For a perfect agreement between model and
13 measurement the CLaMS cloud detections should be exactly at the location where CRISTA
14 observed a cloud. Obviously the model field of IWP shows a good agreement with the cloud
15 occurrence observed by CRISTA. Similar regions show the occurrence of clouds at mid and
16 high latitudes. Some regions are extended larger in the observations than in the model (e.g.
17 the east end of the North Atlantic to Baltic Sea streamer, the extension over Alaska or over
18 Kamchatka). However there are also a few regions where the model shows clouds but the
19 observation is cloud free. But care should be taken in the comparison of model grid and
20 instrument grid data. For example, when the interpolation onto the line of sight is performed
21 numerical errors can generate unrealistically enhanced IWC at altitudes and segments of the
22 line of sight just above the highest grid points with modelled $IWC > 0$. Due to the strong
23 vertical gradients this is especially a problem for IWC and water vapour. Although the
24 comparison look promising, a more quantitative comparison shows that the generated CTHs
25 from the modelled IWP are significantly lower than the observations (not shown) and usually
26 do not reach the LMS (usually between 330 and 350 K and only a few events above, see also
27 section 5.5).

28 In addition, the model is not creating optically very thin cloud layers (low IWP). The
29 probability density function of the modelled IWP extends not significantly below 20 g/m^2 , an
30 indication that the model is not capable to produce optically and/or vertically very thin cirrus
31 cloud layers, which are detectable by an IR limb sounder. Spang et al. (2012) already
32 quantified the detection threshold for IWP to $\sim 0.3 \text{ g/m}^2$. Such small values are rarely observed

1 in the model output, where even values rarely undercut the upper edge of sensitivity in the
2 IWP retrievals of $\sim 20 \text{ g/m}^2$ (larger IWP values are causing optically thick spectra). This ‘high’
3 bias in the modelled IWP is attributed to the freezing parameterisation in the cirrus module of
4 CLaMS. After reaching the over-saturation threshold for ice formation the whole water
5 vapour fraction above 100% saturation over ice is converted into IWC. This approach is an
6 upper limit for ice formation and can overestimate the ‘real’ ice water content. As a result the
7 size of the particles can be over- or underestimated, which consequentially has a strong effect
8 on the dehydration process.

9 **5.5 Zonal Mean cloud occurrence frequencies**

10 For a more quantitative comparison of the cloud occurrence in the model and in the
11 observations we computed the zonal mean cloud top height occurrence frequency in
12 tropopause related coordinates Z_r (see also section 3). For the cloud detection in the model
13 data any line of sight with $\text{IWP} > 0$ is flagged as cloudy and consequently by this approach
14 the highest possible number of clouds will be detected. The zonal means over the whole
15 mission are presented in Figure 9. Overall the distributions from the simulation and
16 observation look very similar. They show a maximum in the tropics well below the
17 tropopause in the observations and slightly higher in altitude and percentages in the model. In
18 addition, a reduced activity in the subtropics for both datasets and very similar COFs around
19 the mid- and high-latitude tropopause are found. However, the CRISTA measurements show
20 substantially increased cloud occurrence frequencies at altitudes well above the tropopause for
21 all latitude bands.

22 The differences in COF between observation and model are illustrated in Figure 9c.
23 Obviously the model overestimates the COF in the tropical upper troposphere and up to
24 slightly above the tropopause, a region defined with the term tropical transition layer
25 (Fueglistaler et al., 2009). Between the isentropic surfaces 350 and 360 K the region of
26 overestimation is extended up to latitudes of 40°N . At these altitudes horizontal transport is
27 possible from tropical and sub-tropical air masses with high water vapour mixing ratios into
28 the LMS to mid and higher latitudes. Since the subtropical jet acts as a transport barrier to
29 meridional transport, this indicates a weakening of the subtropical jet, a condition typically
30 coincident with RWB events in the jet region (Postel and Hitchmann, 1999). RWB events
31 have been observed during the CRISTA-2 mission, like illustrated in Figure 5 and Figure 6 by

1 the development of the PV contours during the mission. Such events are very typical in
2 summer at this altitude and latitude location (e.g. Gabriel and Peters, 2008, Homeyer and
3 Bowman, 2013).

4 Above 360 K in the subtropics and north of 40°N in the tropopause and LMS region CRISTA
5 observations indicate higher COFs than the model and – as already presented in Figure 4 – a
6 large amount of high altitude cloud occurrence in the LMS, which is only weakly present in
7 the model calculations. This is caused by the cirrus module in CLaMS which includes only a
8 simplified approach for ice formation (mainly driven by temperature, the super saturation
9 threshold in respect to ice, specific humidity, and IWC) and is not considering detailed
10 microphysical background or constraint boundary conditions.

11 **5.6 Limb ice water path comparison**

12 This section presents the limb IWP estimated from CRISTA in comparison to CLaMS. As
13 already outlined in section 5.3 the parameters best suited to compare model results with a
14 limb measurement of microphysical information of cirrus cloud are the limb integrated area
15 density and ice water path. IWP_{CLaMS} is computed from the model data following Eq. 2 by
16 using the CLaMS air parcel information of IWC and the limb ray tracing described in section
17 5.4. The zonal mean IWP_{CRISTA} and IWP_{CLaMS} distributions presented in Figure 10 show
18 similar structures like the CTH occurrence frequencies (Figure 9), but include all tangent
19 heights with cloudy signals in the measurements ($IWP > 0$) and in the observations ($CI < 4$
20 equivalent to $IWP > \sim 10^{-3} \text{ g/m}^2$) and not only the CTH locations. For the zonal mean
21 calculation for CLaMS we shortcut all IWP values greater than the upper retrieval limit to
22 $IWP = 20 \text{ g/m}^2$, because clouds with larger IWP are not discriminable in the CRISTA IWP
23 retrieval. By this approach zonal mean values of model and observation become comparable.
24 A good correspondence is found in the zonal mean of IWP_{CRISTA} and IWP_{CLaMS} for altitudes
25 at and below the tropopause, although the CLaMS values tend to be larger than CRISTA
26 when penetrating to lower levels of the troposphere. Only above the tropopause the significant
27 cloud occurrence rates of CRISTA and the vanishing probability to create a cloud in the
28 model become noticeable with means of $IWP_{CRISTA} > IWP_{CLaMS}$. The overall good
29 correspondence below the tropopause is indicating the dominance of optically thicker clouds
30 below the tropopause, whereby the probability for both, model and observation, is much

1 higher to match a similar size of the retrieved IWP values than for the much more variable
2 optical thicknesses of cirrus clouds at and above the tropopause.

3 **5.7 LMS cloud formation in CLaMS**

4 To investigate the process of formation of cirrus clouds in the lowermost stratosphere more
5 closely, results from the CLaMS simulation and additional trajectory calculations are shown
6 for regions where CRISTA observed clouds on August 9 over Scandinavia. Since air masses
7 in CLaMS lose their identity during mixing events, a bundle of backward trajectories was
8 computed starting at the locations of the observations and ending two days earlier near
9 positions, where the last strong mixing occurred. These end points coincide with positions in
10 the vicinity of the subtropical jet over the eastern United States (see Figure 11). Longer
11 backward trajectories are not only more difficult to identify with CLaMS air masses but
12 furthermore end in areas with specific humidities too low to allow for the generation of cirrus
13 clouds. This is due to the low temperatures the air masses experience on their way from the
14 tropics into the mid and higher latitudes.

15 This aspect emphasizes the importance of mixing processes in the vicinity of the subtropical
16 jet, since this increases the water vapour content of the air masses under consideration
17 sufficiently to enable cirrus formation. Longer backward trajectories (without mixing) result
18 in air being too dry. From these positions (two days earlier) cirrus forward simulations with 1
19 hour time step were started. The initialization concerning water vapour and ice water content
20 of the air masses were taken from the background atmosphere as simulated by the CLaMS
21 model. The meteorological conditions concerning temperature and pressure were taken from
22 ERA Interim data.

23 The results of the forward simulations are shown in Figure 12 for all air masses that feature
24 ice formation for the model case with conventional freeze-out at 100% saturation in the
25 above-mentioned area. For a better visualization of the life cycle of the simulated ice clouds,
26 we show results from the start of the trajectories until one day after observation, i.e. August
27 10. The temporal evolution of temperature and potential temperature along the trajectories
28 (Figure 12, top panel) show that about 1 day before observation the air masses underwent a
29 cooling of about 10 K within roughly 6 h, while still moving isentropically. This event
30 coincides with an uplift of about 1 km over the North Atlantic caused by a dynamical low
31 pressure system cut off a trough located to the east (Figure 12, centre panel).

1 Figure 12 (bottom panel) shows the formation of ice initiated by this cooling, setting on
2 earlier for the model case with conventional freeze-out at 100% saturation than for the freeze-
3 out at temperature-dependent over-saturation. Some air masses do not reach enough over-
4 saturation to have freezing started. Those air masses, that feature freezing for both model
5 cases, show similar amounts of gas phase water being converted to ice water. The ice clouds
6 have lifetimes between 14 and 26 hours, and are evaporated 1 day after observation. The
7 vertical positions of the considered air masses are around 400 m above the tropopause height
8 as computed from ERA Interim data.

9 The results from the hemispheric CLaMS simulation (grey areas in Figure 12, bottom panel)
10 show smaller amounts of ice water content than the simulations done with pure trajectories
11 and higher temporal resolution at the time of the observation. This is due to the sedimentation
12 parameterization of particles out of the considered model boxes. The CLaMS results already
13 include the sedimentation of ice for a 24 h time step, while the results of the trajectory-based
14 simulation maintain higher and slowly reducing ice water content during the day. Although
15 this is merely an effect of time resolution, this may explain the fact, that CRISTA
16 observations show higher ice water content than CLaMS.

17 Sensitivity tests with the current setup of CLaMS with changing saturation thresholds for ice
18 formation (100%-150%) and varied radius parameterisations for the sedimentation process
19 did not improve the comparison between model and CRISTA in the LMS. Overall these
20 variations in the setup had little impact on the horizontal and vertical distribution of clouds in
21 the LMS. In addition, temperature fluctuations by gravity waves causing high updraft
22 velocities may play a key role in the nucleation process of ice particles (Spichtinger and
23 Krämer, 2013). These temperature variations need to be considered accurately along the
24 trajectory of an air parcel, but are currently not available for global modelling of cirrus clouds.

25 **6 Summary and Conclusions**

26 A re-analysis of cloud and water vapour measurements during the CRISTA-2 mission in
27 August 1997 in conjunction with model calculations with the Lagrangian chemical transport
28 model CLaMS were presented. Special emphasis was taken to quantify the cloud top altitude
29 with respect to the local tropopause to demonstrate the potential importance of cirrus cloud
30 formation in the lowermost stratosphere above the local tropopause. Little is known about the
31 occurrence frequency and spatial distribution of this particular cloud phenomenon, for

1 example how and why these clouds may form. The occurrence of LMS clouds was previously
2 reported by some lidar stations in the northern hemisphere and occurrence frequencies above
3 the tropopause of a few percent of the total number of cirrus profiles were reported. CRISTA
4 observations extend these local observations to global coverage in the northern hemisphere
5 and show strong indications for frequent cirrus occurrences in the LMS at mid and high
6 latitudes.

7 A reliable hemispheric picture of cloud occurrence in the LMS above the tropopause based on
8 CRISTA-2 observations hinges on an accurate determination of the local tropopause. Here we
9 applied a sophisticated new algorithm to the ERA Interim reanalysis dataset. This so-called
10 high resolution tropopause was compared with TPHs from radiosonde data and showed a
11 good agreement (± 650 m) for more than 5000 selected station profiles in the time frame of the
12 CRISTA-2 mission. This demonstrates the good quality of the ERA Interim temperature
13 profiles around the tropopause.

14 Uncertainties in the determination of the TPH location, instrument specific effects like the
15 potential overestimation of the CTH for optically thick clouds due to the vertical extent of the
16 field of view or uncertainties in the tangent height location were addressed in the present
17 analysis. By quantifying all potential error sources as accurately as possible and modelling the
18 effect of these uncertainties on cloud occurrence frequency statistics in tropopause related
19 coordinates the CRISTA observations show significant numbers of cirrus detections clearly
20 above the local tropopause (500-1500 m) and consequently in the lowermost stratosphere.

21 In general, the cloud top height occurrence frequencies (COF) at the mid-latitude tropopause
22 are in good agreement with the analysis of Pan and Mynchak (2011) based on the spaceborne
23 lidar CALIOP, although these COFs are based on a multi-annual seasonal mean. The
24 CRISTA-2 results show larger COFs than CALIOP above the mid-latitude tropopause (>500
25 m) and also above the tropical tropopause. Overall, rather high occurrence frequencies (~ 5 -
26 10% of all profiles) up to high northern latitudes (70°N) and altitudes well above the
27 tropopause (>350 K) were found in astonishingly large areas of the LMS. These numbers
28 indicate a significantly larger occurrence frequency than in the ground based observations.

29 Further, the northern hemisphere CRISTA water vapour observations indicate a considerable
30 isentropic flux of moisture (at ~ 350 K) from the upper tropical troposphere into the extra-
31 tropical lowermost stratosphere (LMS). This process is triggered by Rossby wave breaking

1 events in the subtropical jet region accompanied by long range transport of high water vapour
2 abundance in streamer and filament structures from the subtropics to mid and high latitudes.
3 The process operates on time scales of few days, is observed at multiple geographical
4 locations starting along the subtropical jet, and is in line with the temporal evolution of PV
5 contours on the respective isentropic layers. Almost all LMS cirrus cloud observations are
6 linked to areas of elongated contour lines of PV and water vapour and indicate an enhanced
7 probability to observe LMS cirrus in the outflow and mixing regions associated with Rossby
8 wave breaking events.

9 Comparisons of the CRISTA-2 measurements with results of CLaMS model simulations,
10 where the model includes modules with parameterised cirrus processes, show a reasonable
11 consistence for the horizontal distribution of cloud patterns in the tropopause region, but
12 differ in the vertical extent of the cloud fields and in the zonal mean occurrence frequency
13 above the tropopause. Significantly less clouds are produced by the model well above the mid
14 and high latitude tropopause than observed.

15 A limb ray tracing approach was applied through the 3D model fields to obtain integrated
16 measurement information through the atmosphere along the limb path of the instrument for a
17 realistic and quantitative comparison of the model results and the measurements. The results
18 confirm a connection between isentropic, quasi-horizontal transport of water vapour from the
19 sub-tropics to the LMS in mid and high latitudes and the occurrence of cirrus clouds in the
20 lowermost stratosphere and tropopause region. However, the simplified cirrus scheme
21 implemented in CLaMS seems to systematically underestimate the cloud occurrence
22 frequencies in the LMS with respect to the observations.

23 Trajectory studies with the cirrus module of CLaMS in comparison with the CLaMS
24 simulations show the importance of mixing for the formation of ice clouds in the LMS.
25 Mixing events at the subtropical jet can generate the entrance of enhanced vapour mixing
26 ratios into the LMS which favour the formation of ice clouds even at high latitudes over
27 Scandinavia in the model in agreement with CRISTA observations.

28 Lidar observations of LMS cirrus above Jülich, Germany (Rolf, 2012) and single cloud events
29 in the CRISTA data set have been modelled along CLaMS trajectories (not shown) with a
30 more sophisticated microphysical bulk model for ice formation (Spichtinger and Gierens,
31 2009a), and for the lidar observations also with a detailed aerosol microphysical model

1 (MAID, Gensch et al., 2008). These preliminary tests could not reproduce the observed cloud
2 structures, although additional temperature fluctuations were taken into account (personal
3 communication C. Rolf and M. Krämer, 2014). Temperature fluctuations may play a key role
4 for a realistic modelling of the formation process of cirrus (Spichtinger and Krämer, 2013),
5 but are difficult to constrain, especially on global scales. Usually temperatures are not low
6 enough and temperature variations are not fast enough to initiate ice formation under the
7 model background conditions. Amongst others, these first attempts of modelling the
8 observations of LMS cirrus indicate that already the meteorological analyses used for the
9 initialisation of water vapour, IWC, and the temperatures along the trajectories, may not
10 include the processes and variability (e.g. gravity waves or small scale and high frequency
11 fluctuations) necessary to generate cirrus clouds in the LMS region. In addition, the formation
12 processes of this specific cirrus cloud type may differ from the current knowledge and
13 implementation in the current microphysical models.

14 Improvements and new developments in the cirrus modules in models as well as multi-
15 instrumental analysis approaches are necessary to achieve progress concerning the questions
16 and unknowns about the formation of cirrus clouds in the LMS. More accurate frequency
17 distribution, seasonal cloud coverage of the northern and southern hemisphere, and
18 microphysical information of LMS cirrus are necessary to quantify the potential radiation and
19 climate impact of LMS cirrus.

20 As a next step, optimised analyses of the currently best suited spaceborne and still operating
21 instrument for cloud studies, the CALIOP instrument on CALIPSO, would help to improve
22 the knowledge on cloud cover and frequency distribution on temporal and spatial scales.
23 Spatial averaging of high resolution CALIOP level 1 data have to be used to improve the
24 detection sensitivity for optically very thin clouds. The unprecedented frequent and
25 statistically significant observation of LMS cirrus by CRISTA may initiate more specific
26 measurement campaigns or model studies with respect to LMS cirrus to quantify the
27 importance of this still intriguing cloud type.

28

29 **Acknowledgements**

30 The authors thank N. Thomas for her excellent programming support during the study.
31 Radiosonde data were kindly provided by L. D. Oolman from the University of Wyoming.

1 ERA Interim data used in this study have been provided by ECMWF. The authors like to
2 thank A. Dudhia, University of Oxford, for providing the radiative transport model RFM, L.
3 Pan, NCAR, for helpful comments on ideas on the tropopause determination based on re-
4 analysis datasets, as well as M. Krämer, B. Vogel, C. Rolf, and F. Ploeger for discussions and
5 comments during the work on the manuscript.

1 **References**

- 2 Avery, M., Winker, D., Heymsfield, A., Vaughan, M., Young, S., Hu, Y., and Trepte, C.:
3 Cloud ice water content retrieved from the CALIOP space-based lidar, *Geophys. Res. Lett.*,
4 19, L05808, doi:10.1029/2011GL050545, 2012.
- 5 Birner, T., Fine scale structure of the extratropical tropopause region, *J. Geophys. Res.*, 111,
6 D04104, doi:10.1029/2005JD006301, 2006.
- 7 Bodas-Salcedo, A., Webb, M. J., Bony, S., Chepfer, H., Dufresne, J.-L., Klein, S. A., Zhang,
8 Y., Marchand, R., Haynes, J. M., Pincus, R., and John, V. O.: COSP: Satellite simulation
9 software for model assessment, *Bull. Amer. Meteor. Soc.*, 92, 1023–1043. doi:
10 <http://dx.doi.org/10.1175/2011BAMS2856.1>, 2011.
- 11 Dee, D. P., Uppala, S. M., Simmons, A. J., Berrisford, P., Poli, P., Kobayashi, S., Andrae, U.,
12 Balmaseda, M. A., Balsamo, G., Bauer, P., Bechtold, P., Beljaars, A. C. M., van de Berg, L.,
13 Bidlot, J., Bormann, N., Delsol, C., Dragani, R., Fuentes, M., Geer, A. J., Haimberger, L.,
14 Healy, S. B., Hersbach, H., Holm, E. V., Isaksen, L., Kallberg, P., Koehler, M., Matricardi,
15 M., McNally, A. P., Monge-Sanz, B. M., Morcrette, J. J., Park, B. K., Peubey, C., de Rosnay,
16 P., Tavolato, C., Thepaut, J. N., and Vitart, F.: The ERA-Interim reanalysis: configuration and
17 performance of the data assimilation system, *Q. J. R. Meteorol. Soc.*, 137, 553-597,
18 doi:10.1002/qj.828, 2011.
- 19 Chepfer, H., S. Bony, D. Winker, G. Cesana, J. L. Dufresne, P. Minnis, C. J. Stubenrauch,
20 and S. Zeng: The GCM Oriented CALIPSO Cloud Product (CALIPSO-GOCCP), *J. Geophys.*
21 *Res.*, 115, D00H16, doi:10.1029/2009JD012251, 2010.
- 22 Davis, S., Hlavka, D., Jensen, E., Rosenlof, K., Yang, Q., Schmidt, S., Bormann, S., Frey, W.,
23 Lawson, P., Voemel, H., and Bui, T. P.: In situ and lidar observations of subvisible cirrus
24 clouds during TC4, *J. Geophys. Res.*, 115, D00J17, doi:10.1029/2009JD013093, 2010.
- 25 Dessler, A. E.: Clouds and water vapor in the Northern Hemisphere summertime stratosphere,
26 *J. Geophys. Res.*, 114, D00H09, doi:10.1029/2009JD012075, 2009.
- 27 Deshler, T., Hervig, M. E., Hofmann, D. J., Rosen, J. M., and Liley, J. B.: Thirty years of in
28 situ stratospheric aerosol size distribution measurements from Laramie, Wyoming (41°N),
29 using balloon-borne instruments, *J. Geophys. Res.*, 108(D5), 4167,
30 doi:10.1029/2002JD002514, 2003.

1 Dionisi, D., Keckhut, P., Liberti, G. L., Cardillo, F., and Congeduti, F.: Midlatitude cirrus
2 classification at Rome Tor Vergata through a multichannel Raman–Mie–Rayleigh lidar,
3 *Atmos. Chem. Phys.*, 13, 11853–11868, doi:10.5194/acp-13-11853-2013, 2013.

4 Dudhia, A., Morris, P. E., and Wells, R. J.: Fast monochromatic radiative transfer calculations
5 for limb sounding, *J. Quant. Spectrosc. Rad. Trans.*, 74, 745–756, 2002.

6 Dupont, J.-C., Haeffelin, M., Morille, Y. Noel, V., Keckhut, P. Winker, D., Comstock, J.,
7 Chervet, P., and Roblin, A.: Macrophysical and optical properties of midlatitude cirrus clouds
8 from four ground-based lidars and collocated CALIOP observations, *J. Geophys. Res.*, 115,
9 D00H24, doi:10.1029/2009JD011943, 2010.

10 Eixmann, R., Peters, D., Zülicke, Ch., Gerding, M., und Dörnbrack, A.: On the upper
11 tropospheric formation and occurrence of high and thin cirrus clouds during anticyclonic
12 poleward Rossby wave breaking events, *Tellus*, 62 A, 228–242, doi:10.1111/j.1600-
13 0870.2010.00437.x, 2010.

14 Fromm, M., Lindsey, D.T., Servranckx, R., Yue, G., Trickl, T., Sica, R., Doucet, P., and
15 Godin-Beekmann, S.: The Untold Story of Pyrocumulonimbus. *Bull. Amer. Meteor. Soc.*, **91**,
16 1193–1209. doi: <http://dx.doi.org/10.1175/2010BAMS3004.1>, 2010.

17 Fusina, F., Spichtinger, P., Lohmann, U.: The impact of ice supersaturated regions and thin
18 cirrus on radiation in the mid-latitudes. *J. Geophys. Res.*, 112, D24S14,
19 doi:10.1029/2007JD008449, 2007.

20 Fischer, H., Birk, M., Blom, C., Carli, B., Carlotti, M., von Clarmann, T., Delbouille, L.,
21 Dudhia, A., Ehhalt, D., Endemann, M., Flaud, J. M., Gessner, R., Kleinert, A., Koopman, R.,
22 Langen, J., López-Puertas, M., Mosner, P., Nett, H., Oelhaf, H., Perron, G., Remedios, J.,
23 Ridolfi, M., Stiller, G., and Zander, R.: MIPAS: an instrument for atmospheric and climate
24 research, *Atmos. Chem. Phys.*, 8, 2151–2188, doi:10.5194/acp-8-2151-2008, 2008.

25 Fueglistaler, S., Dessler, A. E., Dunkerton, T. J., Folkins, I., Fu, Q., and Mote, P. W.: Tropical
26 tropopause layer, *Rev. Geophys.*, 47, RG1004, doi:10.1029/2008RG000267, 2009.

27 Gabriel, A., and Peters, D.: A diagnostic study of different types of Rossby wave breaking
28 events in the northern extra-tropics, *J. Meteor. Soc. Japan*, 86, 613–631, 2008.

1 Griessbach, S., Hoffmann, L., Spang, R., and Riese, M.: Volcanic ash detection with infrared
2 limb sounding: MIPAS observations and radiative transfer simulations, *Atmos. Meas. Tech.*,
3 7, 1487-1507, doi:10.5194/amt-7-1487-2014, 2014.

4 Griessbach, S., Hoffmann, L., Spang, R., von Hobe, M., Müller, R., and Riese, M.: MIPAS
5 Volcanic Sulfate Aerosol Observations of the Nabro Eruption, in: *Stratospheric Sulfur and its
6 Role in Climate (SSiRC)*, Atlanta, Georgia, USA, October 2013, SPARC, available at:
7 <http://www.sparc-ssirc.org/downloads/Griessbach.pdf>, 2013.

8 Gensch, I., Bunz, H., Baumgardner, D., Christensen, L. E., Fahey, D. W., Hermann, R. L.,
9 Lawson, P., Popp, P., Smith, J. B., Webster, C. R., Weinstock, E. M., Wilson, J. C., Peter, T.,
10 Krämer, M.: Supersaturations, Microphysics and Nitric Acid Partitioning in a Cold Cirrus
11 observed during CR-AVE 2006: An Observation-Modeling Intercomparison Study,
12 *Environmental Research Letters* 3, 035003, doi:10.1088/1748-9326/3/3/035003, 2008.

13 Gettelman, A., Hoor, P., Pan, L. L., Randel, W. J., Hegglin, M. I., and Birner, T.: The
14 Extratropical Upper Troposphere and Lower Stratosphere, *Rev. Geophys.*, 49, RG3003,
15 doi:10.1029/2011RG000355, 2011.

16 Gierens, K., Schumann, U., Helten, M., Smit, H. and Wang, P.-H.: Ice-supersaturated regions
17 and subvisible cirrus in the northern midlatitudes upper troposphere, *J. Geophys. Res.*, 105,
18 22743–22753, 2000.

19 Gierens, K. and Spichtinger, P.: On the size distribution of ice-supersaturated regions in the
20 upper troposphere and lowermost stratosphere, *Ann. Geophys.*, 18, 499–
21 504, doi:10.1007/s00585-000-0499-7, 2000.

22 Grossmann, K. U., Offermann, D., Gusev, O., Oberheide, J., Riese, M., and Spang, R.: The
23 CRISTA-2 mission, *J. Geophys. Res.*, 107(D23), 8173, doi:10.1029/2001JD000667, 2002.

24 Hegglin, M. I., Boone, C. D., Manney, G. L., and Walker, K. A.: A global view of the
25 extratropical tropopause transition layer from Atmospheric Chemistry Experiment Fourier
26 Transform Spectrometer O₃, H₂O, and CO, *J. Geophys. Res.*, 114, D00B11,
27 doi:10.1029/2008JD009984, 2009.

28 Höpfner, M., Pitts, M. C., and Poole L. R.: Comparison between CALIPSO and MIPAS
29 observations of polar stratospheric clouds, *J. Geophys. Res.*, 114, D00H05,
30 doi:10.1029/2009JD012114. 2009.

1 Hoffmann, L., and Alexander, M. J.: Occurrence frequency of convective gravity waves
2 during the North American thunderstorm season, *J. Geophys. Res.*, 115, D20111,
3 doi:10.1029/2010JD014401, 2010.

4 Holton, J. R., Haynes, P. H., McIntyre, M. E., Douglass, A. R., Rood, R. B., and Pfister, L.:
5 Stratosphere-troposphere exchange, *Rev. Geophys.*, 33(4), 403–439, doi:10.1029/
6 95RG02097, 1995.

7 Homeyer, C. R., and K. P. Bowman: Rossby Wave Breaking and Transport between the
8 Tropics and Extratropics above the Subtropical Jet, *J. Atmos. Sci.*, 70, 607–626,
9 doi:10.1175/JAS-D-12-0198.1, 2013.

10 Hoor, P., Wernli, H., Hegglin, M. I., and Bönisch, H.: Transport timescales and tracer
11 properties in the extratropical UTLS, *Atmos. Chem. Phys.*, 10, 7929-7944, doi:10.5194/acp-
12 10-7929-2010, 2010.

13 Hoareau, C., Keckhut, P., Noel, V., Chepfer, H., and Baray, J.-L.: A decadal cirrus clouds
14 climatology from ground-based and spaceborne lidars above the south of France (43.9° N–
15 5.7° E), *Atmos. Chem. Phys.*, 13, 6951-6963, doi:10.5194/acp-13-6951-2013, 2013.

16 IPCC: Climate Change 2013 – The Physical Science Basis, Working Group I Contribution to
17 the Fifth Assessment Report of the Intergovernmental Panel on Climate Change, Editor:
18 Intergovernmental Panel on Climate Change, Cambridge University Press, Cambridge, United
19 Kingdom and New York, NY, USA, 2014.

20 Jones, R. L. and Pyle, J. A.: Observations of CH₄ and N₂O by the NIMBUS 7 SAMS: A
21 comparison with in situ data and two dimensional numerical model calculations, *J. Geophys.*
22 *Res.*, 89, 5263-5279, 1984.

23 Jukes, M. N., and McIntyre, M. E.: A high-resolution one-layer model of breaking planetary
24 waves in the stratosphere, *Nature*, 328, 590–596, 1987.

25 Kärcher, B. and Spichtinger, P.: Cloud-controlling Factors of Cirrus, in *Clouds in the*
26 *Perturbed Climate System: Their Relationship to Energy Balance, Atmospheric Dynamics,*
27 *and Precipitation*, Strüngmann Forum Report, volume 2, edited by Jost Heintzenberg and
28 Robert J. Charlson. Cambridge, MA: MIT Press. ISBN-10: 0-262-01287-1, 2009.

1 Keckhut, P., Hauchecorne, A., Bekki, S., Colette, A., David, C., and Jumelet, J.: Indications
2 of thin cirrus clouds in the stratosphere at mid-latitudes, *Atmos. Chem. Phys.*, 5, 3407-3414,
3 doi:10.5194/acp-5-3407-2005, 2005.

4 Kent, G. S., Winker, D. M., Vaughan, M. A., Wang, P.-H., and Skeens, K. M.: Simulation of
5 Stratospheric Aerosol and Gas Experiment (SAGE) II cloud measurements using airborne
6 lidar data, *J. Geophys. Res.*, 102(D18), 21795–21807, doi:10.1029/97JD01390, 1997.

7 Konopka, P., Günther, G., Müller, R., dos Santos, F. H. S., Schiller, C., Ravegnani, F.,
8 Ulanovsky, A., Schlager, H., Volk, C. M., Viciani, S., Pan, L. L., McKenna, D.-S., and Riese,
9 M.: Contribution of mixing to upward transport across the tropical tropopause layer (TTL),
10 *Atmos. Chem. Phys.*, 7, 3285–3308, doi:10.5194/acp-7-3285-2007, 2007.

11 Koop, T.; Luo, B.P.; Tsias, A., Peter, T.: Water activity as the determinant for homogeneous
12 ice nucleation in aqueous solutions, *Nature*, 406, 611-614, 2000.

13 Krämer, M., C. Schiller, C., Afchine, A., Bauer, R., Gensch, I., Mangold, A., Schlicht, S.,
14 Spelten, N., Sitnikov, N., Borrmann, S., de Reus, M., and Spichtinger, P.: Ice supersaturations
15 and cirrus cloud crystal numbers, *Atmos. Chem. Phys.*, 9, 3505-3522, 2009.

16 Kunz, A., Müller, R., Homonnai, V., Jánosi, I. M., Hurst, D., Rap, A., Forster, P. M., Rohrer,
17 F., Spelten, N., and M. Riese, M.: Extending water vapor trend observations over Boulder into
18 the tropopause region: Trend uncertainties and resulting radiative forcing, *J. Geophys. Res.*
19 *Atmos.*, 118, 11,269–11,284, doi:10.1002/jgrd.50831, 2013.

20 Lamquin, N., Stubenrauch, C. J., Gierens, K., Burkhardt, U., and Smit, H.: A global
21 climatology of upper-tropospheric ice supersaturation occurrence inferred from the
22 Atmospheric Infrared Sounder calibrated by MOZAIC, *Atmos. Chem. Phys.*, 12, 381-405,
23 doi:10.5194/acp-12-381-2012, 2012.

24 Luo, B. P., Peter, Th., Wernli, H., Fueglistaler, S., Wirth, M., Kiemle, C., Flentje, H.,
25 Yushkov, V. A., Khattatov, V., Rudakov, V., Thomas, A., Borrmann, S., Toci, G.,
26 Mazzinghi, P., Beuermann, J., Schiller, C., Cairo, F., Di Don-Francesco, G., Adriani, A.,
27 Volk, C. M., Strom, J., Noone, K., Mitev, V., MacKenzie, R. A., Carslaw, K. S.,
28 Trautmann, T., Santacesaria, V., and Stefanutti, L.: Ultrathin Tropical Tropopause Clouds
29 (UTTCs): II. Stabilization mechanisms, *Atmos. Chem. Phys.*, 3, 1093-1100, doi:10.5194/acp-
30 3-1093-2003, 2003.

1 Massie, S., Gille, J., Khosravi, R., Lee, H., Kinnison, D., Francis, G., Nardi, B., Eden, T.,
2 Craig, C., Halvorson, C., Coffey, M., Packman, D., Cavanaugh, C., Craft, J., Dean, V., Ellis,
3 D., Barnett, J., Hepplewhite, C., Lambert, A., Manney, G., Strawa, A., and Legg, M., High
4 Resolution Dynamics Limb Sounder observations of polar stratospheric clouds and subvisible
5 cirrus, *J. Geophys. Res.*, 112, D24S31, doi:10.1029/2007JD008788, 2007.

6 Mahowald, N. M., Plumb, R. A., Rasch, P. J., del Corral, J., and Sassi, F.: Stratospheric
7 transport in a three-dimensional isentropic coordinate model, *J. Geophys. Res.*, 107, 4254,
8 doi:10.1029/2001JD001313, 2002.

9 McKenna, D. S., Konopka, P., Grooß, J.-U., Günther, G., Müller, R., Spang, R., Offermann,
10 D., and Orsolini, Y.: A new Chemical Lagrangian Model of the Stratosphere (CLaMS): 1.
11 Formulation of advection and mixing, *J. Geophys. Res.*, 107, 4309,
12 doi:10.1029/2000JD000114, 2002a.

13 McKenna, D. S., Grooß, J.-U., Günther, G., Konopka, P., Müller, R., Carver, G., and Sasano,
14 Y.: A new Chemical Lagrangian Model of the Stratosphere (CLaMS): 2. Formulation of
15 chemistry scheme and initialization, *J. Geophys. Res.*, 107, 4256,
16 doi:10.1029/2000JD000113, 2002b.

17 Mergenthaler, J., Roche, A.E., Kumer, J.B., and Ely, G.: Cryogenic Limb Array Etalon
18 Spectrometer observations of tropical cirrus, *J. Geophys. Res.*, 104, 22194,
19 doi:10.1029/1999JD900397, 1999.

20 Mitchell, D. L., Rasch, P., Ivanova, D., McFarquhar, G., and Nousiainen, T.: Impact of small
21 ice crystal assumptions on ice sedimentation rates in cirrus clouds and GCM simulations,
22 *Geophys. Res. Lett.*, 35, L09806, doi:10.1029/2008GL033552, 2008.

23 Mitchell, D. L. and Finnegan, W.: Modification of cirrus clouds to reduce global
24 warming. *Environ. Res. Lett.*, 4, 045102, doi:10.1088/1748-9326/4/4/045102, 2009.

25 Montoux, N., P. Keckhut, A. Hauchecorne, J. Jumelet, H. Brogniez, and C. David: Isentropic
26 modeling of a cirrus cloud event observed in the midlatitude upper troposphere and lower
27 stratosphere, *J. Geophys. Res.*, 115, D02202, doi:10.1029/2009JD011981, 2010.

28 Noel, V., and M. Haeffelin: Midlatitude cirrus clouds and multiple tropopauses from a 2002 –
29 2006 climatology over the SIRTa observatory, *J. Geophys. Res.*, 112, D13206,
30 doi:10.1029/2006JD007753, 2007.

1 Offermann, D., K. U. Grossmann, P. Barthol, P. Knieling, M. Riese, and R. Trant, The
2 CRyogenic Infrared Spectrometers and Telescopes for the Atmosphere (CRISTA) experiment
3 and middle atmosphere variability, *J. Geophys. Res.*, 104, 16,311-16,325, 1999.

4 Offermann, D., B. Schaeler, M. Riese, M. Langfermann, M. Jarisch, G. Eidmann, C. Schiller,
5 H. G. J. Smit, and W. G. Read, Water vapor at the tropopause during the CRISTA 2 mission,
6 *J. Geophys. Res.*, 107(D23), 8176, doi:10.1029/2001JD000700, 2002.

7 Pan, L. L., W. J. Randel, B. L. Gary, M. J. Mahoney, and E. J. Hints, Definitions and
8 sharpness of the extratropical tropopause: A trace gas perspective, *J. Geophys. Res.*, 109,
9 D23103, doi:10.1029/2004JD004982, 2004.

10 Pan, L. L., Bowman, K. P., Shapiro, M., Randal, W. J., Gao, R. S., Campos, T., Davis, C.,
11 Schauer, S., Ridley, B. A., Wei, J. C., and Barnett, C.: Chemical behavior of the tropopause
12 observed during the Stratosphere-Troposphere Analyses of Regional Transport experiment, *J.*
13 *Geophys. Res.*, 112, D18110, doi:10.1029/2007JD008645, 2007.

14 Pan, L. L. and L. A. Munchak, Relationship of cloud top to the tropopause and jet structure
15 from CALIPSO data, *J. Geophys. Res.*, 116, D12201, doi:10.1029/2010JD015462, 2011.

16 Peter, Th., Luo, B. P., Wirth, M., Kiemle, C., Flentje, H., Yushkov, V. A., Khatatov, V.,
17 Rudakov, V., Thomas, A., Borrmann, S., Toci, G., Mazzinghi, P., Beuermann, J., Schiller, C.,
18 Cairo, F., Di Donfrancesco, G., Adriani, A., Volk, C. M., Strom, J., Noone, K., Mitev, V.,
19 MacKenzie, R. A., Carslaw, K. S., Trautmann, T., Santacesaria, V., and Stefanutti, L.:
20 Ultrathin Tropical Tropopause Clouds (UTTCs): I. Cloud morphology and occurrence,
21 *Atmos. Chem. Phys.*, 3, 1083-1091, doi:10.5194/acp-3-1083-2003, 2003.

22 Ploeger, F., Fueglistaler, S., Grooß, J.-U., Günther, G., Konopka, P., Liu, Y.S., Müller, R.,
23 Ravegnani, F., Schiller, C., Ulanovski, A., and Riese, M.: Insight from ozone and water
24 vapour on transport in the tropical tropopause layer (TTL), *Atmos. Chem. Phys.*, 11, 407-419,
25 doi:10.5194/acp-11-407-2011, 2011.

26 Ploeger, F., Günther, G., Konopka, P., Fueglistaler, S., Müller, R., Hoppe, C., Kunz, A.,
27 Spang, R., Grooß, J.-U., and Riese, M.: Horizontal water vapor transport in the lower
28 stratosphere from subtropics to high latitudes during boreal summer, *J. Geophys. Res. Atmos.*,
29 118, 8111–8127, doi:10.1002/jgrd.50636, 2013.

1 Postel, G. A., and Hitchman, M. H.: A Climatology of Rossby Wave Breaking along the
2 Subtropical Tropopause. *J. Atmos. Sci.*, 56, 359–373, doi:10.1175/1520-
3 0469(1999)056<0359:ACORWB>2.0.CO;2, 1999.

4 Riese, M., Spang, R., Preusse, P., Ern, M., Jarisch, M., Offermann, D., and Grossmann: K. U.,
5 Cryogenic Infrared Spectrometers and Telescopes for the Atmosphere (CRISTA) data
6 processing and atmospheric temperature and trace gas retrieval, *J. Geophys. Res.*, 104(D13),
7 16349–16367, doi:10.1029/1998JD100057, 1999.

8 Riese, M., Tie, X., Brasseur, G, and D. Offermann, D.: Three-dimensional simulation of
9 stratospheric trace gas distributions measured by CRISTA, *J. Geophys. Res.*, 104(D13),
10 16419–16435, doi:10.1029/1999JD900178, 1999a.

11 Riese, M., Manney, G. L., Oberheide, J., Tie, X., Spang, R., and Kull, V.: Stratospheric
12 transport by planetary wave mixing as observed during CRISTA-2, *J. Geophys. Res.*, 107,
13 8179, doi:101029/2001JD000629, 2002.

14 Riese, M., Ploeger, F., Rap, A., Vogel, B., Konopka, P., Dameris, M., and Forster, P.: Impact
15 of uncertainties in atmospheric mixing on simulated UTLS composition and related radiative
16 effects, *J. Geophys. Res.*, 117, D16305, doi:10.1029/2012JD017751, 2012.

17 Rohs, S., Schiller, C., Riese, M., Engel, A., Schmidt, U., Wetter, T., Levin, I., Nakazawa, T.,
18 and Aoki, S.: Long-term changes of methane and hydrogen in the stratosphere in the period
19 1978-2003 and their impact on the abundance of stratospheric water vapor, *J. Geophys. Res.*,
20 111, 1-12, doi:10.1029/2005JD006877, 2006.

21 Rolf, C., Lidar observations of natural and volcanic-ash-induced cirrus clouds, *Schriften des*
22 *Forschungszentrum Jülich, Reihe Energie & Umwelt, Band 163, Jülich, 2013.*

23 Sanderson, B. M., Piani, C., Ingram, W. J., Stone, D. A., Allen, M. R.: Towards constraining
24 climate sensitivity by linear analysis of feedback patterns in thousands of perturbed-physics
25 GCM simulations, Volume 30, Issue 2-3, pp 175-190, *Climate Dynamics*, 2008.

26 Sassen, K., M. K. Griffin, and G. C. Dodd, Optical scattering and microphysical properties of
27 subvisible cirrus clouds, and climatic implications, *J. Appl. Meteorol.*, 28, 91– 98, 1989.

28 Schaeler, B. and Riese, M.: Retrieval of water vapor in the tropopause region from CRISTA
29 measurements, *Adv. Space Res.*, 27(10), 1635-1640, doi:10.1016/S0273-1177(01)00228-9,
30 2001.

1 Schaeler, B., Offermann, D., Kuell, V., Jarisch, M., Feldmann, H., and A. Ebel, A.: Regional
2 and global trace gas distributions and inferred transports in the upper troposphere and lower
3 stratosphere, *J. Geophys. Res.*, 110, D09104, doi:10.1029/2004JD004994, 2005.

4 Sembhi, H., Remedios, J., Trent, T., Moore, D. P., Spang, R., Massie, S., and Vernier, J.-P.:
5 MIPAS detection of cloud and aerosol particle occurrence in the UTLS with comparison to
6 HIRDLS and CALIOP, *Atmos. Meas. Tech.*, 5, 2537-2553, doi:10.5194/amt-5-2537-2012,
7 2012.

8 Solomon, S., Rosenlof, K., Portmann, R., Daniel, J., Davis, S., Sanford, T., and Plattner, G.-
9 K.: Contributions of stratospheric water vapor to decadal changes in the rate of global
10 warming, *Science*, 327, 1219-1223, doi:10.1126/science.1182488, 2010.

11 Spang, R., Riese, M., and Offermann, D.: CRISTA-2 observations of the south polar vortex in
12 winter 1997: A new data set for polar process studies, *Geophys. Res. Lett.*, 28, 3159-3162,
13 2001.

14 Spang, R., Eidmann, G., Riese, M., Offermann, D., Preusse, P., Pfister, L., and Wang, P. H.:
15 CRISTA observations of cirrus clouds around the tropopause, *J. Geophys. Res.*, 107, 8174,
16 doi:10.1029/2001JD000698, 2002.

17 Spang R., and Remedios, J.: Observations of a distinctive infra-red spectral feature in the
18 atmospheric spectra of polar stratospheric clouds measured by the CRISTA instrument,
19 *Geophys. Res. Lett.*, 30, 1875, doi:10.1029/2001JD000698, 2003.

20 Spang, R., Remedios, J. J., and Barkley, M.: Colour Indices for the Detection and
21 Differentiation of Cloud Types in Infra-red Limb Emission Spectra, *Adv. Space Res.*, 33,
22 pp.1041–1047, 2004.

23 Spang, R., Remedios, J. J., Kramer, L. J., Poole, L. R., Fromm, M. D., Müller, M.,
24 Baumgarten, G., and Konopka, P.: Polar stratospheric cloud observations by MIPAS on
25 ENVISAT: detection method, validation and analysis of the northern hemisphere winter
26 2002/2003, *Atmos. Chem. Phys.*, 5, 679-692, doi:10.5194/acp-5-679-2005, 2005a.

27 Spang, R., Remedios, J. J., Tilmes, S., and Riese, M., MIPAS observation of polar
28 stratospheric clouds in the Arctic 2002/2003 and Antarctic 2003 winters, *Adv. Space Res.*, 36,
29 pp.868–878, 2005b.

1 Spang, R., Hoffmann, L., Kullmann, A., Olschewski, F., Preusse, P., Knieling, P.,
2 Schroeder, S., Stroh, F., Weigel, K., Riese, M., High resolution limb observations of clouds
3 by the CRISTA-NF experiment during the SCOUT-O3 Tropical Aircraft campaign, *Adv.*
4 *Space Res.*, 42 (2008), pp. 1765–1775, 2007.

5 Spang, R., Arndt, K., Dudhia, A., Höpfner, M., Hoffmann, L., Hurley, J., Grainger, R. G.,
6 Griessbach, S., Poulsen, C., Remedios, J. J., Riese, M., Sembhi, H., Siddans, R., Waterfall,
7 A., and Zehner, C.: Fast cloud parameter retrievals of MIPAS/Envisat, *Atmos. Chem. Phys.*,
8 12, 7135–7164, doi:10.5194/acp-12-7135-2012, 2012.

9 SPARC, Assessment of Stratospheric Aerosol Properties (ASAP), Thomason, L. W. and T.
10 Peter, Eds., SPARC Report No. 4, WCRP-124, WMO/TD, No. 1295, [http://www.sparc-](http://www.sparc-climate.org/publications/sparc-reports/sparc-report-no4/)
11 [climate.org/publications/sparc-reports/sparc-report-no4/](http://www.sparc-climate.org/publications/sparc-reports/sparc-report-no4/), 2006.

12 Spichtinger, P., Gierens, K., Leiterer, U., and Dier, H.: Ice supersaturation in the tropopause
13 region over Lindenberg, Germany, *Meteorol. Z.*, 12, 143–156, 2003a.

14 Spichtinger, P., Gierens, K., and Read, W.: The global distribution of ice-supersaturated
15 regions as seen by the Microwave Limb Sounder, *Q. J. Roy. Meteor. Soc.*, 129, 3391–3410,
16 2003b.

17 Spichtinger, P. and Gierens, K. M.: Modelling of cirrus clouds – Part 1a: Model description
18 and validation, *Atmos. Chem. Phys.*, 9, 685-706, doi:10.5194/acp-9-685-2009, 2009a.

19 Spichtinger, P. and Gierens, K. M.: Modelling of cirrus clouds – Part 1b: Structuring cirrus
20 clouds by dynamics, *Atmos. Chem. Phys.*, 9, 707-719, doi:10.5194/acp-9-707-2009, 2009b.

21 Spichtinger, P. and Krämer, M.: Tropical tropopause ice clouds: a dynamic approach to the
22 mystery of low crystal numbers, *Atmos. Chem. Phys.*, 13, 9801-9818, doi:10.5194/acp-13-
23 9801-2013, 2013.

24 Tuck, A. F., Baumgardner, D., Chan, K. R., Dye, J. E., Elkins, J. W., Hovde, S. J., Kelly, K.
25 K., Loewenstein, M., Margitan, J. J., May, R. D., Podolske, J. R., Prott, M. H., Rosenlof, K.
26 H., Smith, W. L., Webster, C. R., and Wilson, J. C.: The Brewer-Dobson circulation in the
27 light of high altitude in situ aircraft observations. *Quarterly Journal of the Royal*
28 *Meteorological Society*, 123, 1-69, DOI: 10.1002/qj.49712353702, 1997.

29 von Hobe, M., Groöß, J.-U., Gunther, G., Konopka, P., Gensch, I., Kramer, M., Spelten, N.,
30 Afchine, A., Schiller, C., Ulanovsky, A., Sitnikov, N., Shur, G., Yushkov, V., Ravegnani, F.,

1 Cairo, F., Roiger, A., Voigt, C., Schlager, H., Weigel, R., Frey, W., Borrmann, S., Muller, R.,
2 and Stroh, F.: Evidence for heterogeneous chlorine activation in the tropical UTLS, *Atmos.*
3 *Chem. Phys.*, 11, 241-256, 2011.

4 Wang, P. H., Minnis, P., McCormick, M. P., Kent, G. S., and Skeens, K. S., A 6-year
5 climatology of cloud occurrence frequency from SAGE II observations (1985–1990), *J.*
6 *Geophys. Res.*, 101, 29,407– 29,429, 1996.

7 Wang, T., and A. E. Dessler: Analysis of cirrus in the tropical tropopause layer from
8 CALIPSO and MLS data: A water perspective, *J. Geophys. Res.*, 117, D04211,
9 doi:10.1029/2011JD016442, 2012.

10 Wattenbach, R., and Moritz, K., Astronomical shuttle pallet satellite (ASTRO-SPAS), *Acta*
11 *Astronautica*, Volume 40, Issue 10, 723–732, 1997.

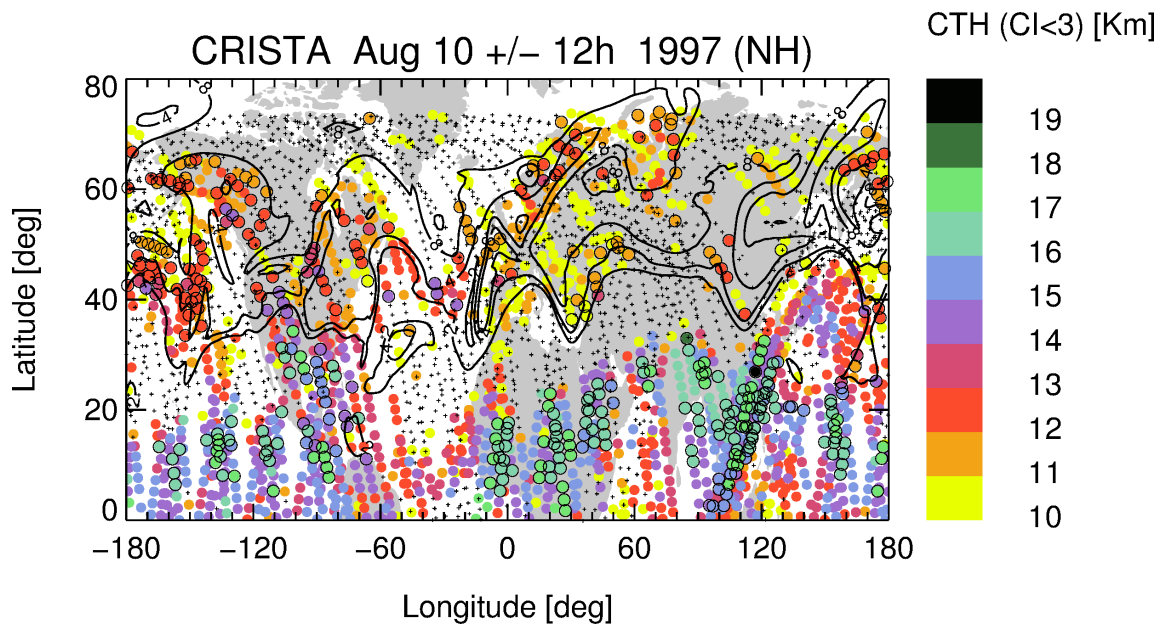
12 Wendisch, M., P. Yang, and P. Pilewskie: Effects of ice crystal habit on thermal infrared
13 radiative properties and forcing of cirrus. *J. Geophys. Res.*, 112, D08201,
14 doi:10.1029/2006JD007899, 2008.

15 Winker, D. M., Vaughan, M. A., Omar, A. H., Hu, Y., Powell, K. A., Liu, Z., Hunt, W. H.,
16 and Young, S. A.: Overview of the CALIPSO Mission and CALIOP Data Processing
17 Algorithms, *J. Atmos. Ocean. Tech.*, 26, 2310–2323, doi:10.1175/2009JTECHA1281.1, 2009.

18 World Meteorological Organization (WMO): Meteorology a three-dimensional Science:
19 Second Session of the commission for Aerology, *WMO Bulletin IV(4)*, WMO, Geneva, 134–
20 138, 1957.

21 Wooster, M. J., Perry, G. L. W., and Zoumas, A.: Fire, drought and El Niño relationships on
22 Borneo (Southeast Asia) in the pre-MODIS era (1980–2000), *Biogeosciences*, 9, 317-340,
23 doi:10.5194/bg-9-317-2012, 2012.

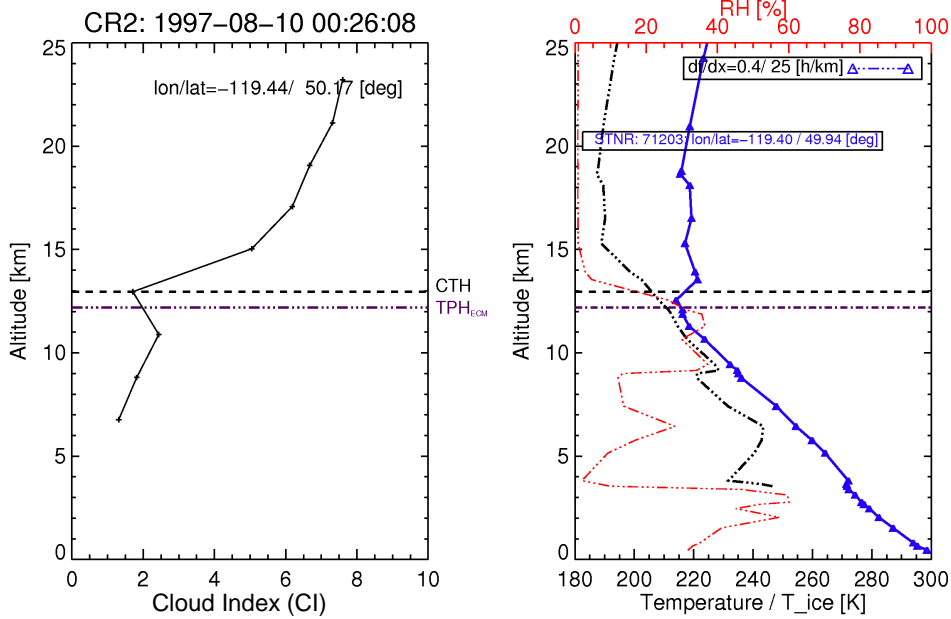
24 Zhang, M. H., Lin, W. Y., Klein, S.A., Bacmeister, J., Bony, S., Cederwall, R. T., Del Genio,
25 A., Hack, J. J., Loeb, N., Lohmann, U., Minnis, P., Musat, I., Pincus, R., Stier, P., Suarez, M.
26 J. Webb, J., Xie, S. C., Yao, M. and Zhang, J. H.: Comparing clouds and their seasonal
27 variations in atmospheric general circulation models with satellite measurements, *J. Geophys.*
28 *Res.*, 110, D15S02, doi:10.1029/2004JD005021, 2005.



1

2 Figure 1: CRISTA cloud top height distribution for 1997 Aug 10 00:00 UTC +/- 12 hours
 3 (coloured circles). Profiles with no cloud indications are marked by black crosses. Overlaid in
 4 black are contours of potential vorticity at 2, 4, and 8 PVU at the 350 K isentrope. Cloud tops
 5 with PV values greater than the proxy threshold 2 PVU for the dynamical tropopause are
 6 highlighted by black borders of the coloured circles for CTH.

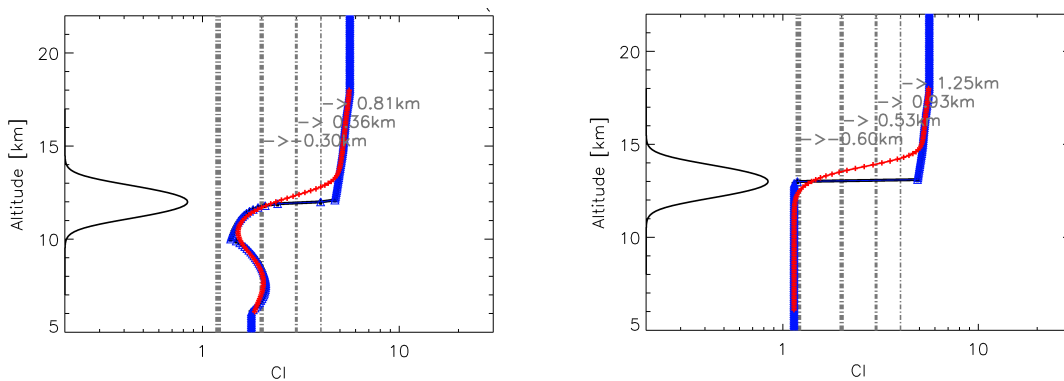
1



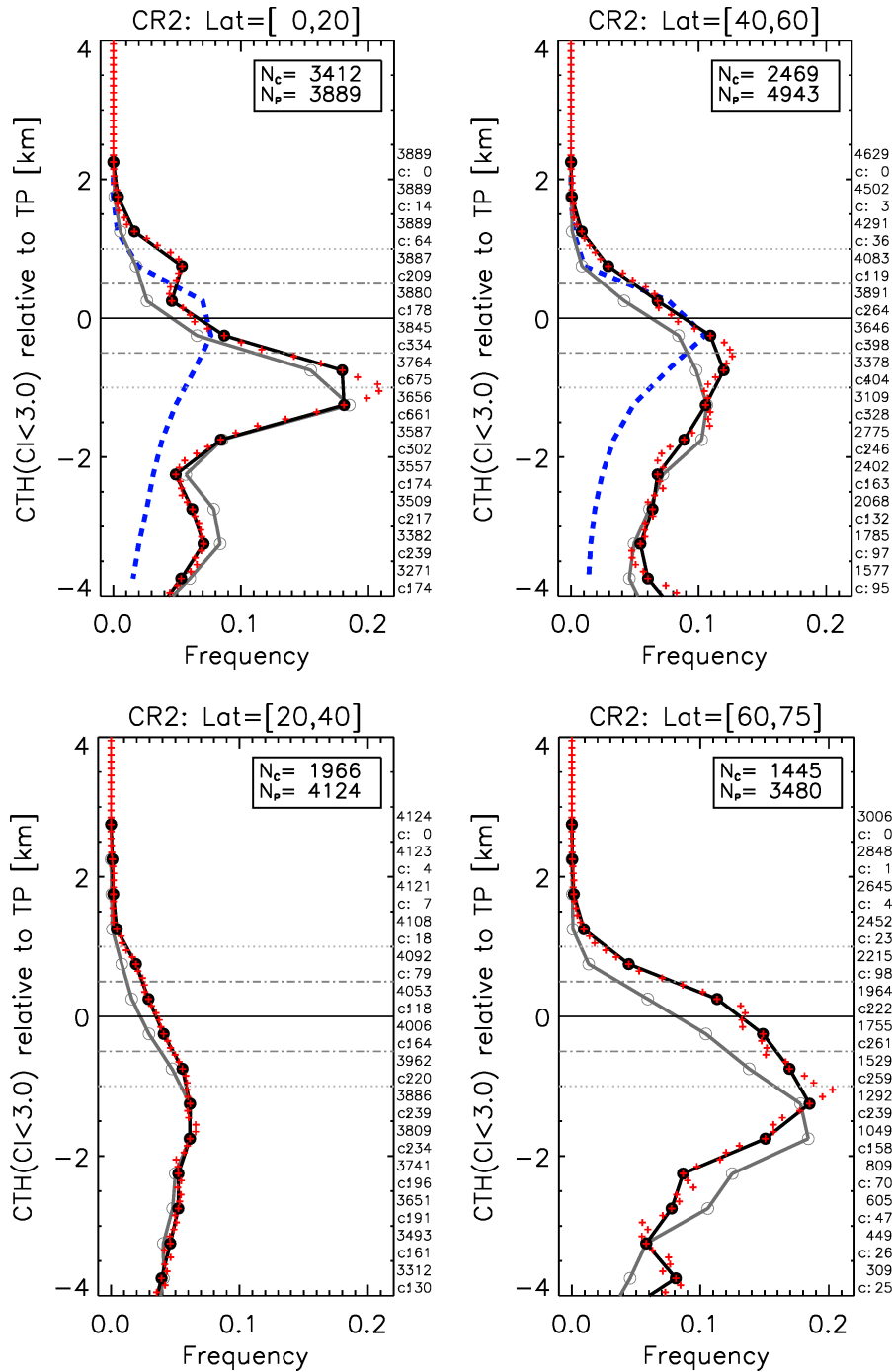
2 Figure 2: Cloud index (CI) profile during CRISTA-2 (left) and coincident radiosonde
 3 measurements (right) at mid-latitudes. The profiles on the right side show temperature (blue)
 4 and relative humidity (red). The ice saturation temperature curve is superimposed by the
 5 black-dash-dotted curve. Horizontal lines indicate cloud top height (CTH) from the CRISTA
 6 measurements (dashed) and the so-called 'high resolution' tropopause height (TPH_{HR}) from
 7 ERA Interim temperature data (dash-dotted), for details see section 2.5.

8

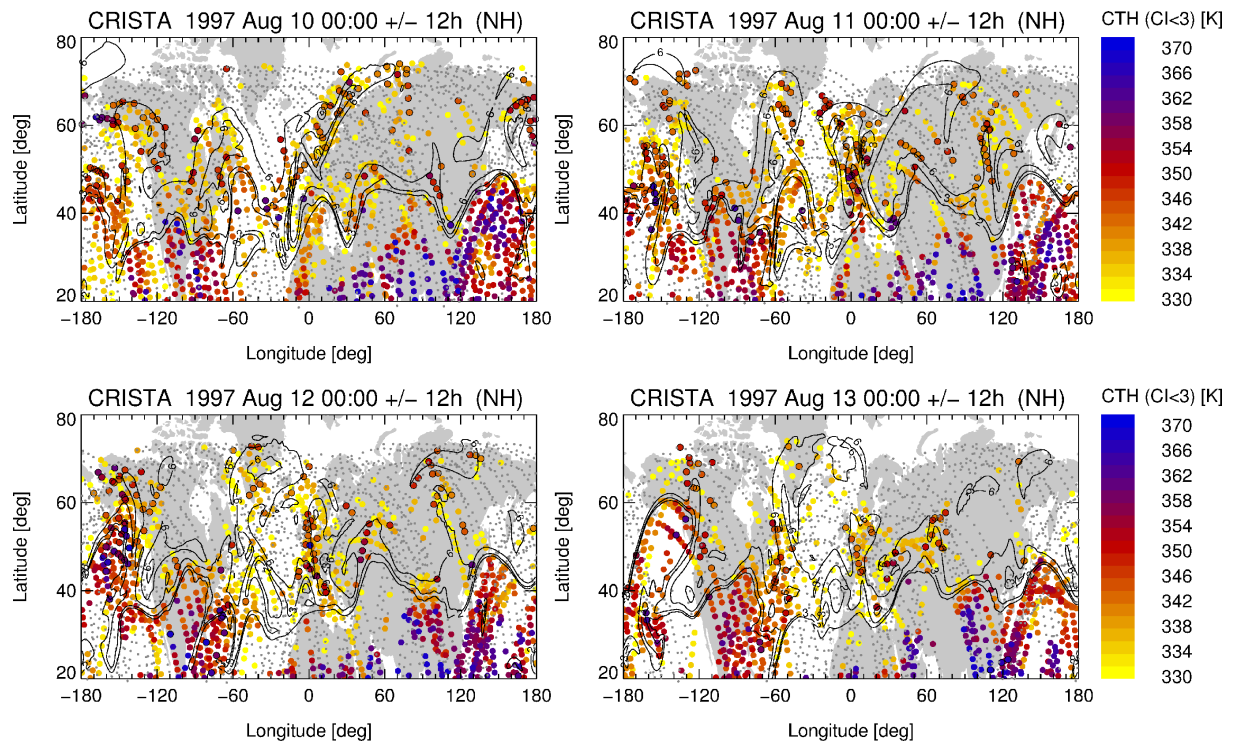
9



10 Figure 3: Examples of cloud index profile computed from modelled radiance profiles with
 11 high vertical resolution (0.1 km, in blue) for a 2 km thick cloud layer with cloud top at 12 and
 12 13 km for optically thin (left) and thick (right) conditions respectively. The Gaussian shaped
 13 field of view was applied to the pencil beam simulations (blue) to simulate CRISTA profiles
 14 (red) (examples of the FOV function are centred at the cloud top at 12 and 13 km). The
 15 superimposed numbers indicate the maximum errors in CTH, $dCTH=[\text{no detection}, -0.30,$
 16 $0.36, 0.81]$ km (left) and $dCTH=[-0.56, 0.53, 0.94, 1.28]$ km (right) for the corresponding CI
 17 threshold values [1.2, 2, 3, 4] applied in the cloud detection.



2 Figure 4: Cloud occurrence frequencies of CTHs relative to the tropopause for four latitude
 3 bands and the two detection thresholds $CI_{thres}=2$ (grey circles) and $CI_{thres}=3$ (black dots). The
 4 numbers at the right y-axis are highlighting the number of observations (top number) and the
 5 number of CTH counts (c:) in the corresponding altitude grid box (500 m) for $CI_{thres}=3$. Blue
 6 dashed line in the top two figures represents the JJA mean COF values for CALIPSO in the
 7 time frame June 2006 to May 2010 (taken from Fig. 10 in PM2011). Uncertainty limits of \pm
 8 0.5 and 1 km are presented by the horizontal lines. Red symbols represent a 100 m running
 9 mean statistic of 500 m vertical boxes.

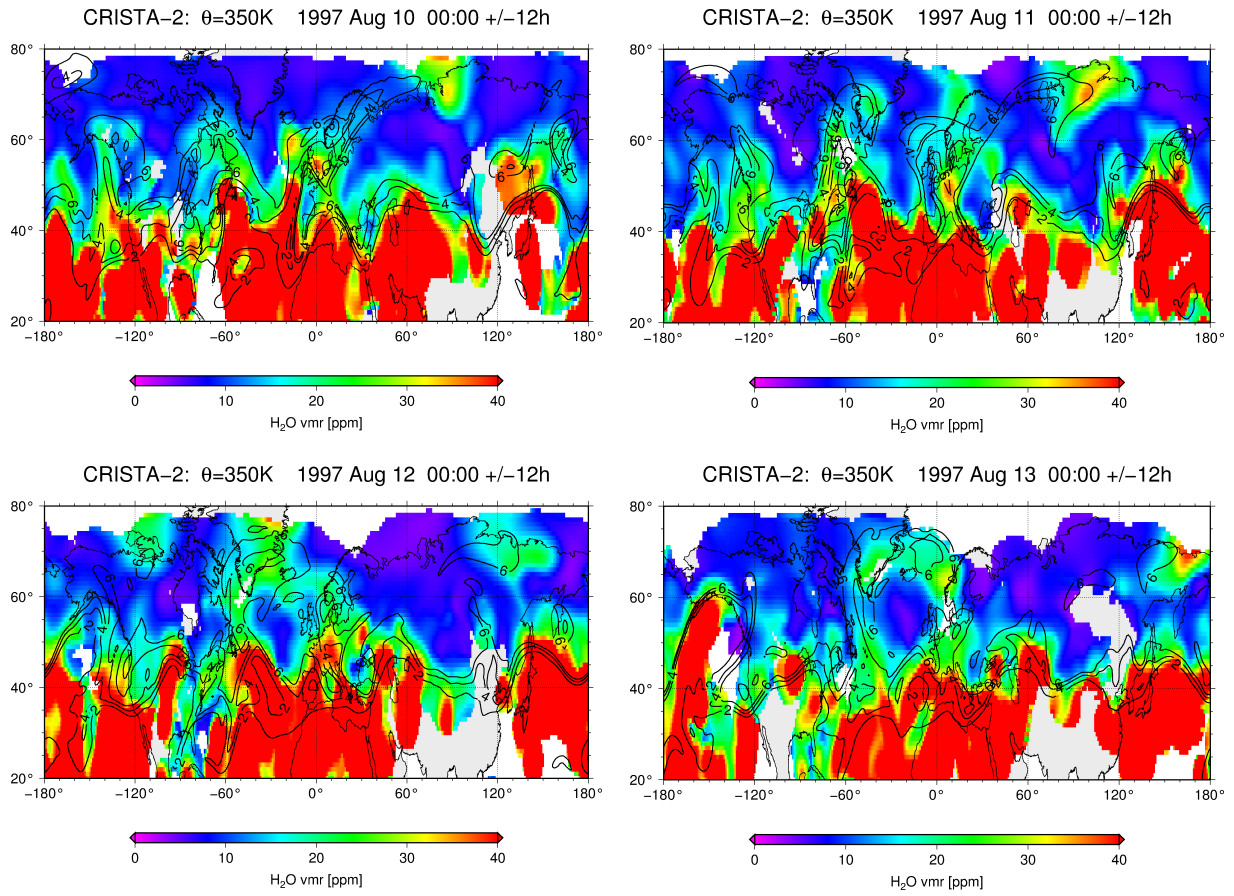


1

2 Figure 5: CRISTA-2 daily detection of cloud top heights on vertical Θ -coordinates between
 3 330 and 370 K (colour coded) from August 10 to 13 at 00:00 +/- 12 hours. Black circles
 4 around the coloured symbols mark CTH observation above the local tropopause. Potential
 5 vorticity contours for 2, 3, and 6 PVU are overlaid in black at midnight conditions. In addition
 6 horizontal wind contours for 30 and 40 m/s (in green) are highlighting the subtropical jet as
 7 well as regions with fast horizontal transport at higher latitudes. Crosses are marking non-
 8 cloudy profiles in the Θ -range 330 to 370 K.

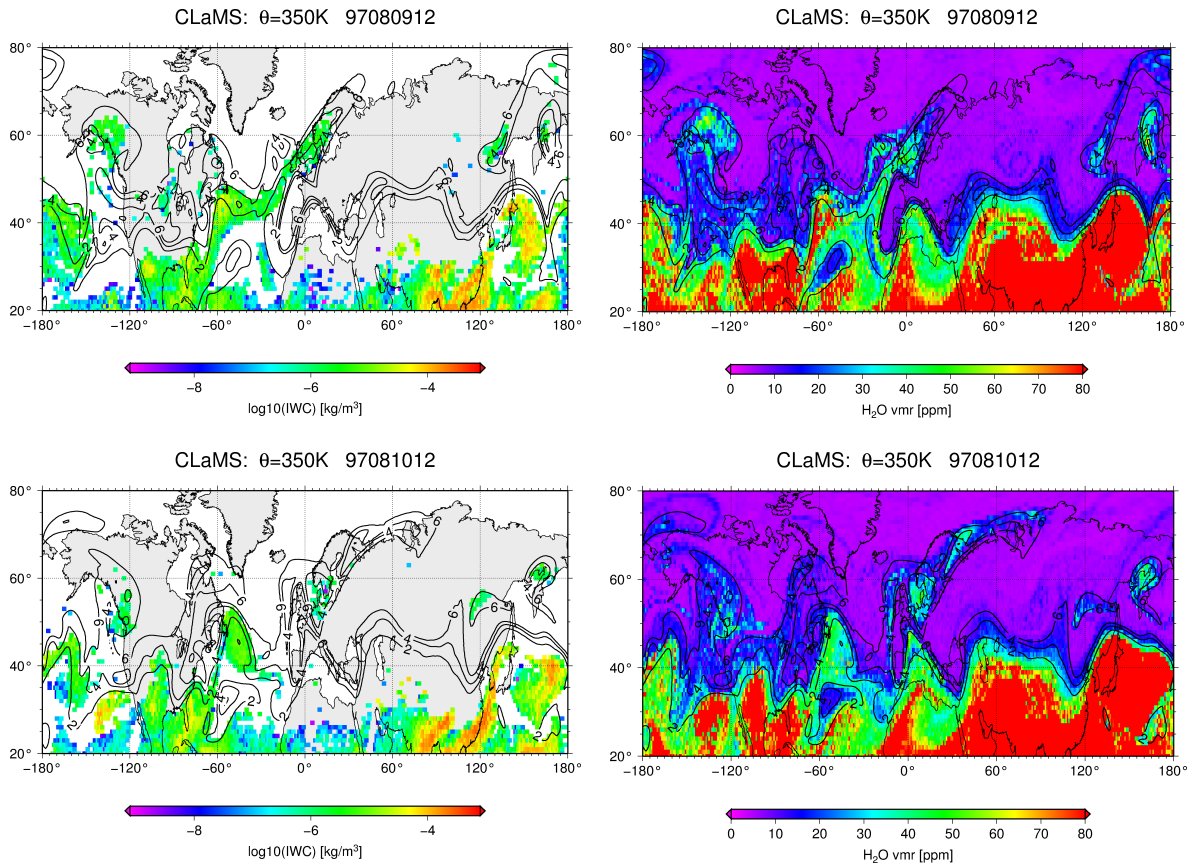
9

1



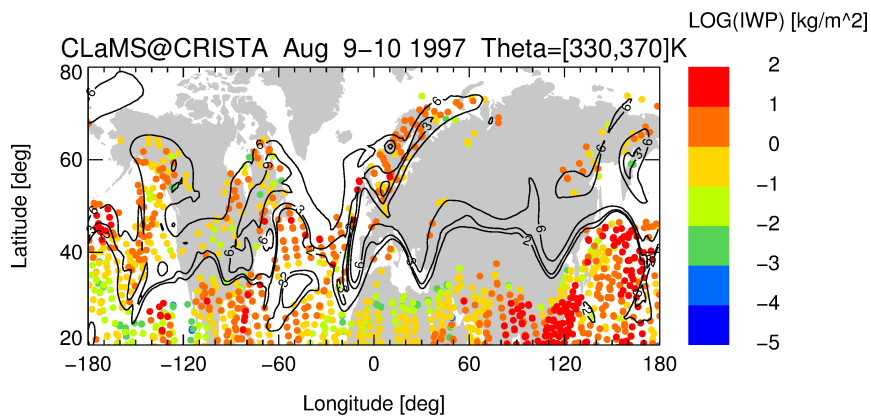
2 Figure 6: CRISTA 2 measurements of water vapour for August 10 to 13 00:00 +/- 12 hours.
3 The asynoptic measurements are interpolated spatially to a regular grid (for details see text).
4 In addition, PV contour lines of 2, 4, and 8 PVU are overlaid in black. White patches in the
5 water distribution indicate data gaps due to clouds.

1



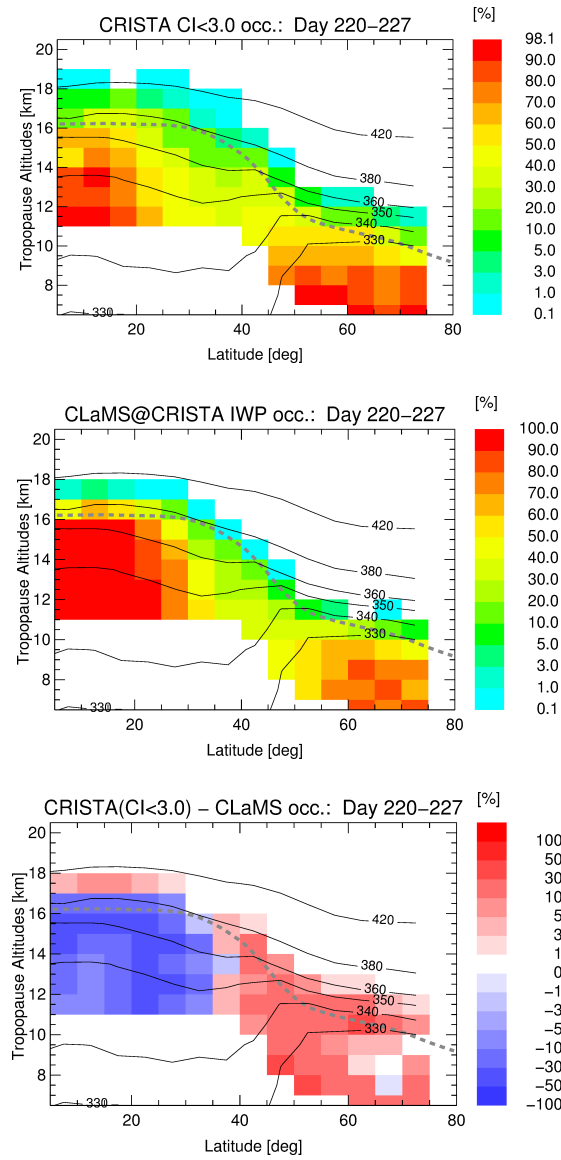
2 Figure 7: CLaMS model results of IWC (left) and water vapour (right) for meteorological
 3 input data based on ERA Interim, top row for the 9th of August 12:00 and bottom row for the
 4 10th of August 1997. CLaMS irregular data are interpolated to a 1° x 1° grid for the 350 K
 5 isentrope.

6



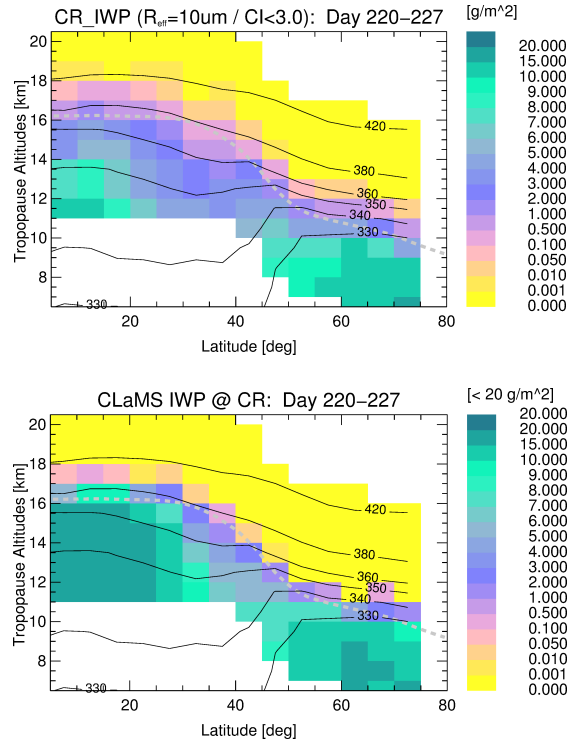
7 Figure 8: Limb ice water path based on derived from CLaMS IWC integrated along CRISTA
 8 line of sights for 10 Aug 1997 00:00 +/- 12 hours between the 330 and 370 K isentrope (for
 9 details see text). PV contours for 2, 3, and 6 PVU are superimposed.

10



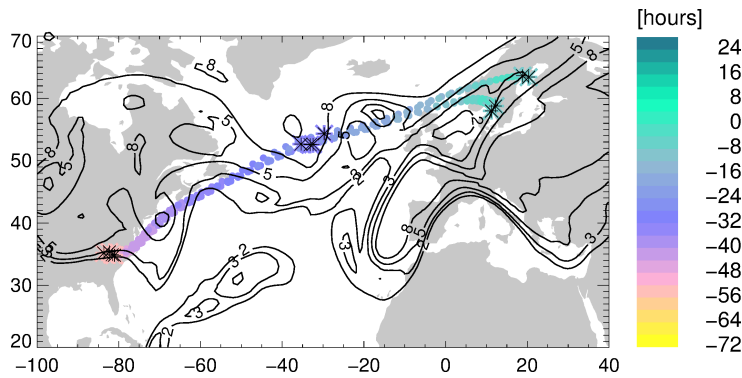
1 Figure 9: Cloud top height occurrence frequencies in tropopause related vertical coordinates
 2 for the complete measurement period (7 days) of CRISTA-2 (top) based on $CI_{\text{thres}}=3$, the
 3 corresponding CLaMS model is sampled with line of sights of CRISTA, and cloud top
 4 detection is based on $IWP > 0$ (middle). Differences in cloud top height occurrence frequency
 5 between CRISTA and CLaMS sampled with CRISTA are presented in the bottom diagram.
 6 Contours for zonal mean isentropes (black) and for the zonal mean tropopause altitude
 7 (dashed grey) are superimposed.

8



1
2
3
4
5
6
7
8

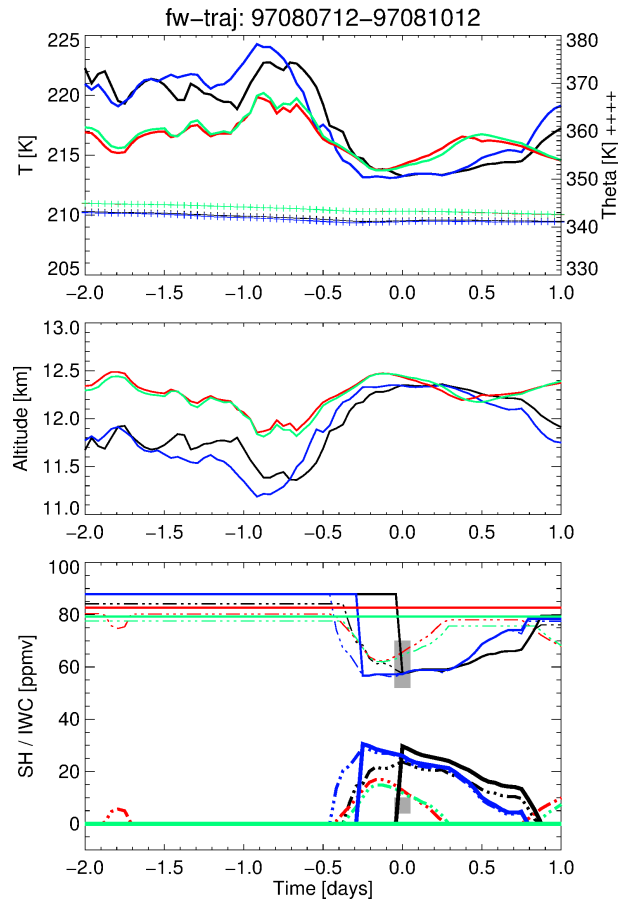
Figure 10: Zonal mean CRISTA limb IWP retrieved from CI (top) and from the CLaMS model (bottom) with a shortcut of $IWP_{CLaMS} > 20 \text{ g/m}^2$ at the upper detection sensitivity of CRISTA (right). For the computation of IWP_{CR} it is necessary to assume a constant effective radius for the ice particles ($R_{eff} = 10 \mu\text{m}$ is applied, see also Eq. 2).



9
10

Figure 11: Geographical position of four forward trajectories from August 7 12:00 to August 9 12:00 (coloured dots) based on 2-day backward trajectories from CLaMS ice events over Scandinavia ($IWC > 0$ and altitudes above the tropopause) at August 9 12:00 (reference time for Figure 12). PV contours are presented at $\Theta = 350 \text{ K}$ for August 9 12:00. Crosses mark the position at August 7, 8, and 9 12:00.

1



2

3 Figure 12: Forward trajectory calculations with respect to the reference time August 9 12:00
4 (-2 days to +1 day) with 1 hour temporal resolution. **Top:** the panel shows temperature and
5 isentropic temperature (crosses) versus time for the four trajectories of Figure 11; **middle:**
6 altitude information; **bottom:** specific humidity (thin lines) and ice water content (thick lines
7 below 40 ppmv) of the CLaMS cirrus module. In addition, SH and IWC for the conventional
8 freeze-out at 100% saturation (dash-dotted lines) are superimposed. Grey shaded areas
9 indicate IWC and SH range in the original 24h time step CLaMS model run at the reference
10 time.

11